applied sciences

MDPI

Review

Recent Advances in Non-Traditional Elastic Wave Manipulation by Macroscopic Artificial Structures

Jeonghoon Park [1], Dongwoo Lee [1] and Junsuk Rho [1,2,*]

[1] Department of Mechanical Engineering, Pohang University of Science and Technology (POSTECH), Pohang 37673, Korea; jh2park@postech.ac.kr (J.P.); dwlee93@postech.ac.kr (D.L.)

[2] Department of Chemical Engineering, Pohang University of Science and Technology (POSTECH), Pohang 37673, Korea

* Correspondence: jsrho@postech.ac.kr; Tel.: +82-54-279-2187

Received: 29 November 2019; Accepted: 8 January 2020; Published: 11 January 2020

Abstract: Metamaterials are composed of arrays of subwavelength-sized artificial structures; these architectures give rise to novel characteristics that can be exploited to manipulate electromagnetic waves and acoustic waves. They have been also used to manipulate elastic waves, but such waves have a coupling property, so metamaterials for elastic waves uses a different method than for electromagnetic and acoustic waves. Since researches on this type of metamaterials is sparse, this paper reviews studies that used elastic materials to manipulate elastic waves, and introduces applications using extraordinary characteristics induced by metamaterials. Bragg scattering and local resonances have been exploited to introduce a locally resonant elastic metamaterial, a gradient-index lens, a hyperlens, and elastic cloaking. The principles and applications of metasurfaces that can overcome the disadvantages of bulky elastic metamaterials are discussed.

Keywords: elastic metamaterial; phononic crystals; gradient-index lens; elastic hyperlens; elastic cloaking; elastic metasurface

1. Introduction

A metamaterial (MTM) is an artificial composite material or structure that has physical properties rarely found in nature. They are constructed by repeatedly arranging man-made micro-structures. Adjustments to the shape, size and arrangement of the micro-components can give unique characteristics such as negative parameters that cannot exist in conventional materials. The concept of MTMs was proposed by Victor Veselago [1]; he predicted that a material that had simultaneous negative electric permittivity (ϵ) and negative magnetic permeability (μ) would have a negative refractive index (n). Subsequently, negative n was realized in electromagnetic metamaterials (EM-MTMs) [2] by embedding metallic structures appropriately to achieve effective negative ϵ and μ. Since then, EM-MTMs have been applied to various fields such as super-resolution imaging [3–5], invisibility cloaking [6–8] and sensing [9–12]. Acoustic metamaterials (AMTMs) can be also implemented by adjusting the effective density (ρ) and bulk modulus (B) [13]. ρ is analogous to ϵ, and compressibility ($\kappa = 1/B$) is analogous to μ. More details can be found in [14] showing the exact duality of constitutive components in between two different fields at cylindrical coordinates. Studies of AMTMs that exploit the mechanisms used in EM-MTMs have also been conducted [15,16]. Elastic metamaterials (EMTMs) can generate elastic waves with meta-characteristics, but this application is impeded by some special characteristics of elastic waves. Electromagnetic waves generally have two transverse modes (transverse electric (TE) and transverse magnetic (TM)), and acoustic waves have only one longitudinal mode. However, elastic waves propagate as vibrational motion of a solid medium, so they have both transverse and longitudinal modes concurrently to be considered. This coupling of transverse and longitudinal modes does not occur in electromagnetic waves and acoustic waves in the linear approximation, so the techniques used in electromagnetism or acoustics cannot be applied directly to EMTMs. Therefore, relevant research on EMTMs has been conducted [17].

EMTMs can manipulate elastic waves by exploiting either Bragg scattering or local resonance. Bragg scattering causes a strong destructive effect on the propagation of scattered waves within a medium when the distance between two scatterers is one-half of the wavelength. At frequencies that meet this condition, a bandgap occurs, in which the real-valued wavevector is forbidden, so waves cannot propagate. Local resonances in a micro-structure can yield negative ρ or negative stiffness K if significant deformation is applied. Therefore, a local resonator within the micro-structure must be designed to suppress dynamic external behavior and prevent wave propagation. If a synthetic substance has either negative ρ or negative K, then waves within that substance have an imaginary-valued velocity, so they attenuate rather than propagate or reflect. These novel characteristics of EMTMs lead to various applications such as passive vibration attenuation systems [18–25], active vibration attenuation systems [26–29], energy harvesters [30–32], energy dissipation systems [33,34], seismic barriers [35–42], viscoelastic systems [43,44], non-reciprocal elastic wave propagation systems [45–47], gyroscopic metamaterials [48,49] and elastic topological phononic crystals [50,51].

In this review, we discuss the theoretical and experimental development of applications using EMTMs in five sections. In Section 2.1, we introduce representative studies of locally resonant EMTMs. In Section 2.2, we explain the gradient-index lens (GRIN) implemented by phononic crystals. In Section 2.3, we introduce super-resolution techniques that use EMTM hyperlenses. In Section 2.4, we provide the mechanism of elastic cloaking using MTMs. Finally, in Section 3, we describe different approaches to achieve elastic metasurfaces. We wrap up by giving our views on possible applications.

2. Elastic Metamaterials

2.1. Representative Studies of Locally Resonant Elastic Metamaterials

Locally resonant EMTM uses motions of micro-structures exploiting the coupling effect of local oscillators. The most widely used method is the effective medium theory (EMT) in order to directly estimate the behavior of them. EMT in a homogenized scheme has been achieved by analyzing scattering coefficients, so that effective parameters such as effective mass density, ρ, bulk modulus, κ, and shear modulus, μ can be obtained solely possessing reliance on the filling ratio with respect to the host and inclusion in a matrix at the long wavelength limit within EMTMs [52,53]. The other method is the S-parameter retrieval method (SPRM) that numerically extracts effective parameters through scattering components by a toy model. Notice that only a handful of studies on SPRM in EMTMs exists, and one can be found that effective mass density and stiffness have been investigated considering full anisotropy with intrinsic nonlocal responses in the system [54].

One hybrid EMTM that exhibits two different characteristics depends on operation frequency has been proposed [55]. The proposed EMTM consists of multi-mass locally resonant units which can generate monopolar, dipolar and quadrupolar resonances. In the higher frequency negative dispersion band, only pressure waves can be transferred. In the lower frequency negative dispersion band, compressional waves and shear waves can only propagate in different directions. These novel properties greatly extend the ability to control elastic waves. A two-dimensional EMTM, including fluid-solid composites, which can have negative shear modulus and negative mass density over a large frequency domain has been proposed [56]. The unit cell of proposed EMTM consists of a lattice of rubber-coated water cylinders (Figure 1a). This composite can generate both dipolar and quadrupolar resonances in its structures, so negative shear modulus and negative mass density can be realized. Negative effective refractive index appears in the regime (Figure 1b A to B) where both mass density and shear modulus have negative value. Negative refraction caused by a negative effective refractive index has been demonstrated by multiple-scattering theory simulations (Figure 1c). In addition, mode conversion from transverse waves to longitudinal waves was observed under negative refraction conditions. An EMTM with chiral micro-structures has been also demonstrated to achieve subwavelength negative refraction [57]. Three ribs of the unit cell induce translational resonance as well as rotational resonance about the central piece. Therefore, by selecting the dimension of the chirally distributed ribs, simultaneous translational and rotational resonances and negative refraction at a low-frequency range can be achieved. Negative refraction of the longitudinal elastic wave at the deep-subwavelength scale was experimentally and numerically demonstrated. This EMTM can be used for elastic wave focusing. One locally resonant EMTM that exhibits polarization bandgaps has been designed [58]; it consists of three-dimensional anisotropic locally resonant units (Figure 1d). The polarization bandgaps allow selective suppression of vibration modes. In particular, a unique property of fluids was observed; the frequency region where all flexural vibrations are suppressed, but longitudinal vibration is allowed (Figure 1e). In addition, the frequency region where torsional vibration can be significantly suppressed was observed (Figure 1f). This EMTM can be used for separating and controlling elastic waves of different polarizations.

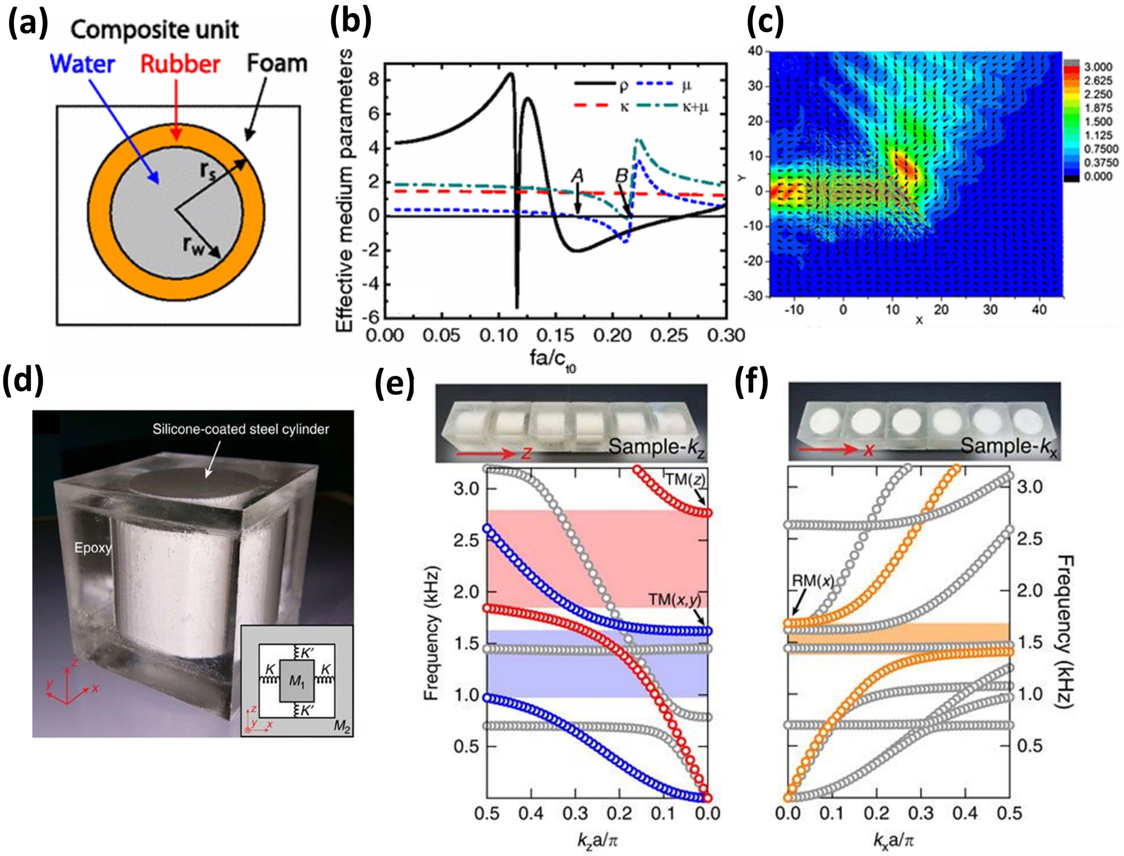

Figure 1. (**a**) Unit cell of the locally resonant elastic metamaterial (EMTM); (**b**) Effective medium parameters of proposed EMTM. Black line: mass density, ρ. Blue line: shear modulus, μ. Red line: bulk modulus, κ. Green line: κ + μ; (**c**) Total flux distribution for a transverse wave incidence on the wedge. Colors: the magnitude. Black Arrows: directions; (**d**) Unit cell design of a locally resonant EMTM; (**e**) The band structure of z-axis alligned EMTM. Blue shaded region: a flexural bandgap. Red shaded region: a longitudinal bandgap; (**f**) The band structure of x-axis alliged EMTM. Orange shaded region: a torsional bandgap. (**a**–**c**) adapted from [56]. (**d**–**f**) adapted from [58].

2.2. Elastic Gradient-Index Lens Using Phononic Crystals

Phononic crystals (PCs) are artificial structures that are composed of periodic structures, and that exhibit complete or partial frequency bandgaps of elastic or acoustic waves. The main difference between a PC and an MTM arises from the geometric size of the structure [59,60]. In the case of MTM, the size and periodic spacing of the micro-components are very small compared to the wavelength of waves passing through them. However, for PCs, the periodic spacing of the structures is similar to the wavelength. As mentioned in the introduction, these gaps can be used to create band gaps through Bragg scattering. Due to the importance of bandgap properties, investigating the frequency bandgaps has been a large part of work on PCs. Since the pioneering work by Kushwaha et al. [61], PCs have been studied due to their unique physical properties and their ability to manipulate the propagation of elastic waves. The properties of PCs have potential applications such as sensors [62–65], filters [66–68] and waveguides [69–71]. In particular, gradient-index (GRIN) PCs designed as another application have a refractive index (n) that gradually decreases outwards from the center (Figure 2a); they were developed for elastic focusing. In a GRIN PC, an incident wave gradually tends to bend toward the center axis at which n is highest, and eventually converges to the focal point with no aberration following the Lagrangian viewpoint in terms of particle tracking. This focusing phenomenon has many practical applications such as flat lenses for detection and imaging. In comparison, some examples of GRIN lenses that do not exploit PCs will be introduced.

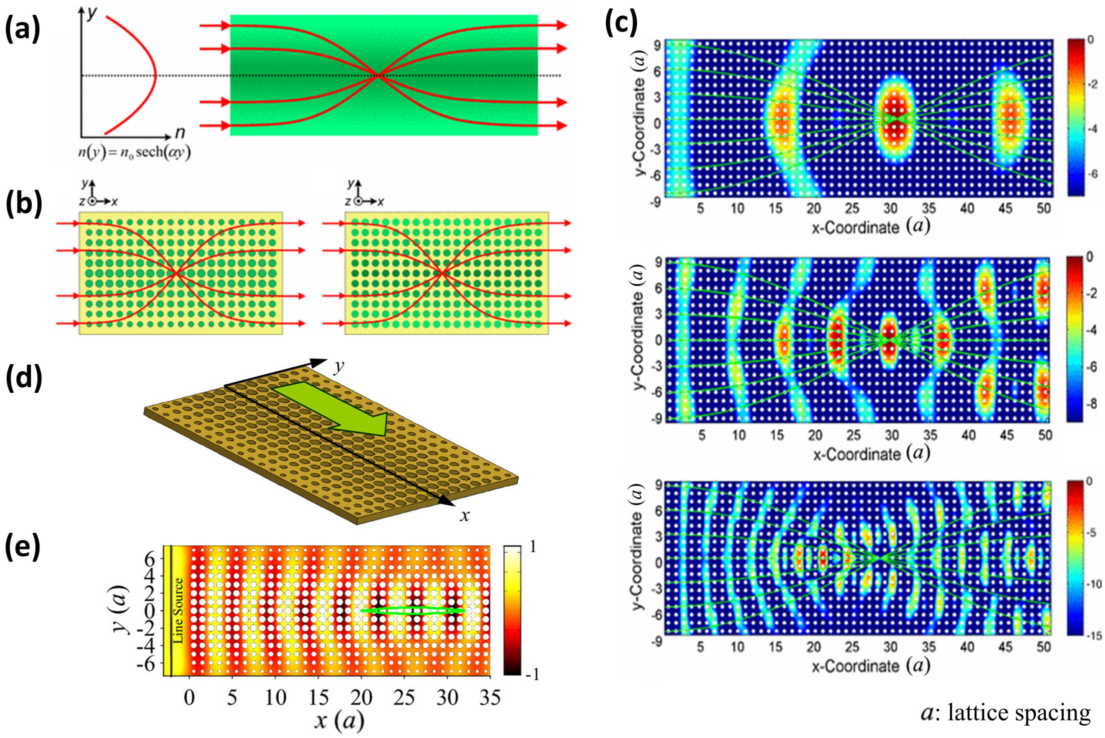

Figure 2. (**a**) Schematic diagram of the principle of a gradient-index (GRIN) lens. Red arrow: incident beams; (**b**) GRIN Phononic crystal (PC) realized by adjusting radius of cylinders (left). GRIN PC realized by changing elastic properties of cylinders (right); (**c**) Finite-Difference Time-Domain (FDTD) simulation of displacement fields when wave propagates in the GRIN PC at a reduced frequency of $\Omega = 0.05$ (top), $\Omega = 0.10$ (center) and $\Omega = 0.20$ (bottom); (**d**) Schematic of the GRIN PC plate. Green arrow: wave propagation direction; (**e**) Displacement amplitude along the x direction measured at 3 MHz. Green contour: area where amplitude > 0.95 times maximum value. (**a**–**c**) adapted from [72]. (**d**,**e**) adapted from [73].

The first GRIN PCs lens was composed of solid cylinders embedded in an epoxy medium [72]. The refractive index profiles along the direction transverse to the wave propagation has a formula with hyperbolic secant function; this gradient enables redirection of incident waves and focusing. The GRIN PC can be realized by controlling n by adjusting the radii of cylinders in each layer or by changing elastic properties of cylinders (Figure 2b). The GRIN PC allows acoustic waves to converge over a broad range of operating frequencies (Figure 2c). The following studies of GRIN PCs for elastic waves mainly considered the propagation of Lamb waves, which propagate in solid plates. The particle motion in Lamb waves is perpendicular to the direction of propagation. Many modes of particle motion exist, but the two most common modes are the symmetric S0 mode and the antisymmetric A0 mode. These two modes are important because they carry more energy than the higher-order modes in most cases. A GRIN PC in a silicon plate (Figure 2d) can focus the lowest-order antisymmetric A0 Lamb wave (Figure 2e) [73]. This work was extended to optimize GRIN PC plate design to get a refractive index gradient that has an approximately parabolic profile and to focus the zero-order antisymmetric A0 Lamb wave within a broadband frequency region; the finite-element method and a laser-ultrasonic technique were used to numerically and experimentally demonstrate sub-wavelength focusing of Lamb waves that had frequencies of 7–10 MHz [74]. GRIN PC plates for focusing and waveguiding of the Lamb wave A0 without a waveguide (Figure 3a) and with a waveguide (Figure 3b) have been demonstrated numerically and experimentally [75]; a piezoelectric AT-cut quartz was used as the material of the plane. The inaccuracy of the location of maximum focusing between the simulation and experiment may occur from the hole etching. This study may enable development of an active GRIN PC plate device based on a piezoelectric substrate. GRIN PCs in plates can control both S0 and A0 Lamb waves simultaneously (Figure 3c) in a wide frequency range [76]. Another device that uses a GRIN PC in which air holes were scattered in a silicon substrate (Figure 3d) has been proposed [77]; the focusing of a Rayleigh wave was experimentally demonstrated (Figure 3e) using a laser ultrasonic technique.

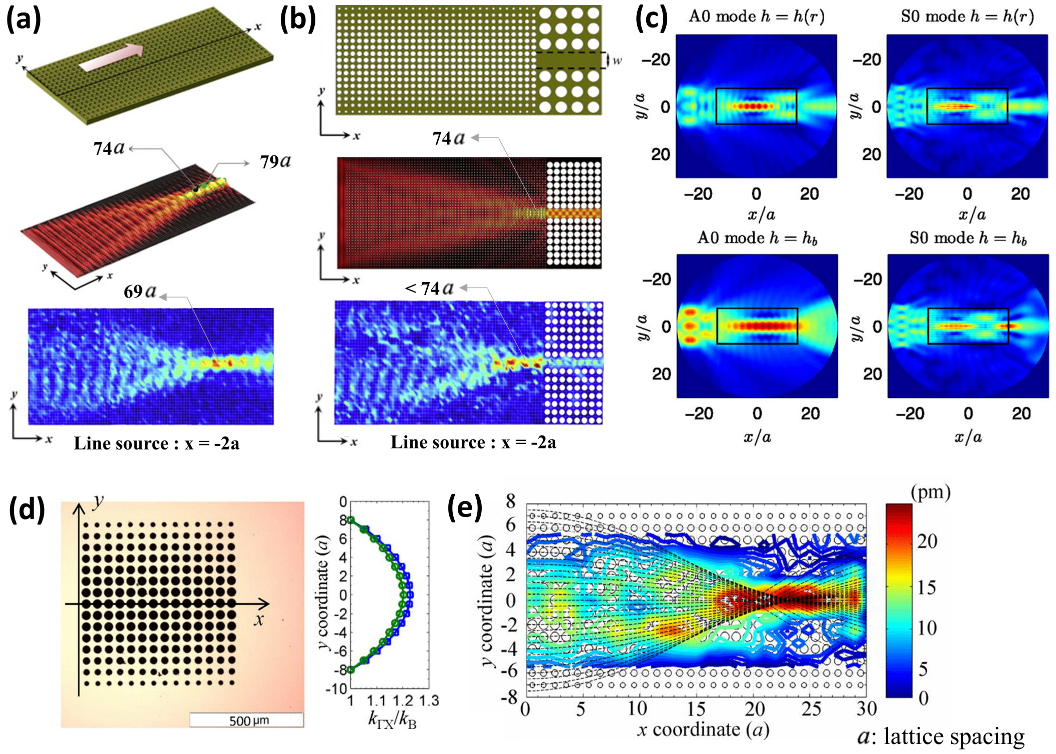

Figure 3. (**a**) GRIN PC plate on an AT-cut quartz plate (top). Arrow: wave propagation direction (x axis). The simulation of focusing of the lowest A0 mode in the designed GRIN PC lens (center). The measured amplitude distributions of the GRIN PC plate lens at 10 MHz (bottom); (**b**) Same as (**a**) but a linear waveguide is added; (**c**) Upper side: Normalized field distribution for a A0-polarized (left) and a S0-polarized (right) plane waves where the thickness of the plate is designed to focus the two Lamb modes simultaneously. Lower side: same as the upper side but the thickness of the plate is constant; (**d**) GRIN PC on a silicon plate with a thickness 500 µm (left) with simulated (blue squares) and experimental (green circles) values of the effective refractive index (right); (**e**) Experimental maximum of out-of-plane displacement in GRIN PC lens. Dashed black lines: ray trajectories. (**a**,**b**) adapted from [75]. (**c**) adapted from [76]. (**d**,**e**) adapted from [77].

One GRIN lens without using PCs was made by adjusting the thickness of the plate [78]. The desired n was obtained by designing n to increase as the thickness of the lens decreases. Three kinds of GRIN lens, Luneburg lens, Maxwell fish-eye lens, 90° lens were introduced and numerically demonstrated [79]. Unlike PCs or using thickness variation of the plate, this study uses resonant EMTM to design GRIN lenses. A Luneburg lens is a GRIN lens in which n decreases radially from the center to the perimeter, expressed as

$$n(r) = \sqrt{(2 - (r/R)^2}, \tag{1}$$

where R and r denotes the radius of the sphere and the radial distance measured from the center of the sphere. A Maxwell fish-eye lens is a GRIN lens that focuses the point on the spherical edge to another point on the opposite edge when a point source is located at the edge of the sphere. n varies according to the relation expressed as

$$n(r) = \frac{2}{1 + (r/R)^2}, \tag{2}$$

where R and r have the same meaning as in Equation (1). 90° rotating lens is a GRIN lens which rotates a ray about 90°. The relationship between r and n in this lens is written as

$$rn^4 + 2n + 1 = 0. \tag{3}$$

Note that the extended version for an arbitrary rotating lens called generalized Eaton lens has theoretically been introduced [80], and experimentally been conducted [81] in the acoustic regime by exploiting the index profile described as

$$n(r, \phi) = \left(\frac{2R}{r} - 1\right)^{\phi/(\pi+\phi)}, \tag{4}$$

for $r < R$. ϕ is the arbitrary desired refraction angle.

The focusing of elastic waves in plates can be used in to harvest energy by collecting the energy of elastic waves. Numerical and experimental studies demonstrated that GRIN PCs that use blind holes and are coupled with piezoelectric transduction can improve the harvesting of elastic waves [82]. This concept was extended [83] to create a GRIN lens with continuously-varying index profile by gradually altering the rigidity properties to focus and harvest flexural waves. The GRIN lens coupled to piezoelectric harvesters can efficiently focus and harvest waves at the designed fixed focal points and work well in a broad frequency range (Figure 4a,b). The focal harvester was better than the baseline harvester (Figure 4c). One Luneburg lens enables precise focusing of an omnidirectional plane wave (Figure 4d,e); the harvested power output by a Luneburg lens was more than 10 times higher than by the baseline harvester (Figure 4f) [84].

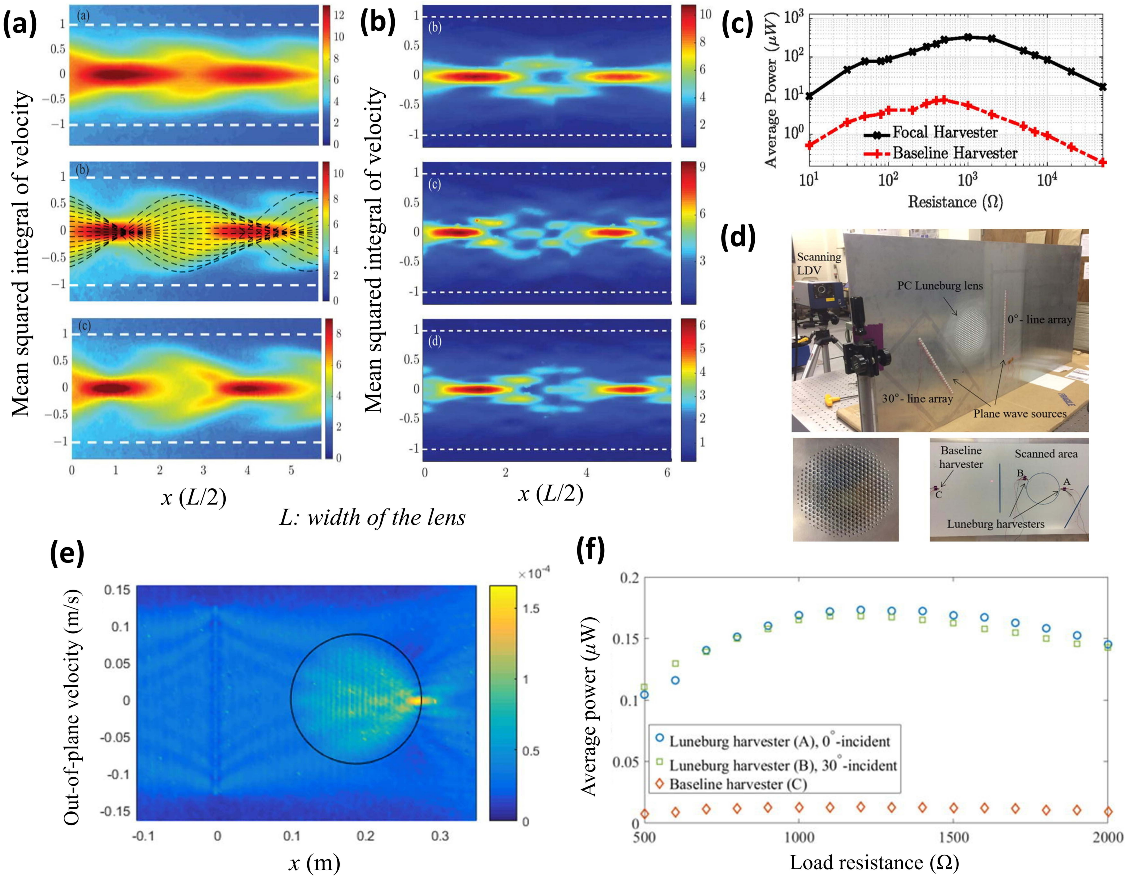

Figure 4. (**a**) Non-dimensionalized mean-squared integral of velocity generated by line source excitation for 20 kHz (top), 40 kHz (center), and 60 kHz (bottom). The focal points match the ray-theory simulation in the center figure; (**b**) Corresponding experiment results using a 100-kΩ resistor at (top) 20 kHz, (center) 40 kHz, and (bottom) 60 kHz. Dashed white line: outer edges of the lens; (**c**) Average power generated by the GRIN lens of load resistance at 40 kHz; (**d**) (top) Experimental apparatus, (lower left) close-up view of the PC lens sample. (lower right) Locations of the Luneburg harvesters and the baseline harvester; (**e**) Experimental root mean square (RMS) wave fields for incidence of (top) 0°; (**f**) Average power generated by the PC Luneburg harvesters and baseline harvester. (**a**–**c**) adapted from [83]. (**d**–**f**) adapted from [84].

2.3. Elastic Hyperlens

Light that is emitted or scattered from an object, is composed of two components: a propagating component that is composed of low wavevectors, and an evanescent component that is composed of high wavevectors. The propagating wave encodes large feature information, and can propagate to the far-field, whereas the evanescent wave encodes fine features, but its power decays exponentially in a conventional environment and cannot reach the far-field. Because of this property of the evanescent component, realization of sub-wavelength imaging is a big challenge in a general sense. This problem can be solved using hyperlenses constructed by MTMs with strong anisotropy. A hyperlens has very large or unbounded cutoff wavevectors, so it can support the propagation of an evanescent wave to the far-field [85–87]. This hyperlens shows a remarkable potential for applications, such as biomedical imaging, nanolithography and optical sensing. The first hyperlens concept was derived from EM-MTMs [88]. The device is non-resonant, so is unconstrained in terms of material loss. One acoustic hyperlens does not use local resonance accompanied by negative effective parameters [89]; this design has been used to demonstrate hyperlenses that have elliptical equi-frequency contours (EFCs) in the elastic regime, and therefore have very strong anisotropy [90]. However, elliptical EFCs have limited resolution because their wavevectors are still bounded despite having higher cutoff wavevectors than spherical EFCs. One solution to this problem is to use hyperbolic EFCs that have unbounded wavevectors.

EFCs shows the wave vectors along the propagation direction of waves at the same frequency. The propagation direction of each wave is perpendicular to EFCs with distinct figuration, so diffraction characteristics can be predicted. The characteristics of spherical EFCs, elliptic EFCs and hyperbolic EFCs are distinct (Figure 5). In spherical EFCs in an isotropic medium, a cutoff wavevector (k_c) limits the spatial frequency along the tangential direction (θ), so a diffraction limit occurs. In a hyperlens that uses an elliptic EFC, the magnitude of k_c increases due to the strong anisotropy, so sub-wavelength imaging is possible. However, when the magnitude of the circumferential wavevector (k_θ) becomes larger than the magnitude of k_c, the information contained in wavevector cannot be transmitted along the radial direction r because radial wavevector (k_r) becomes imaginary. In a hyperlens that uses hyperbolic EFCs, the real-valued k_r enables k_θ to become very large, because the cutoff wavevector is unbounded, so the wave components of the large circumferential wavevectors k_θ can propagate along the r direction. Therefore, evanescent waves that have high spatial frequency and cannot be resolved by a conventional lens, are converted to propagating waves. Thus, the hyperbolic EFC hyperlens enables super-resolution sub-wavelength imaging to strengthen the evanescent waves and imaging features.

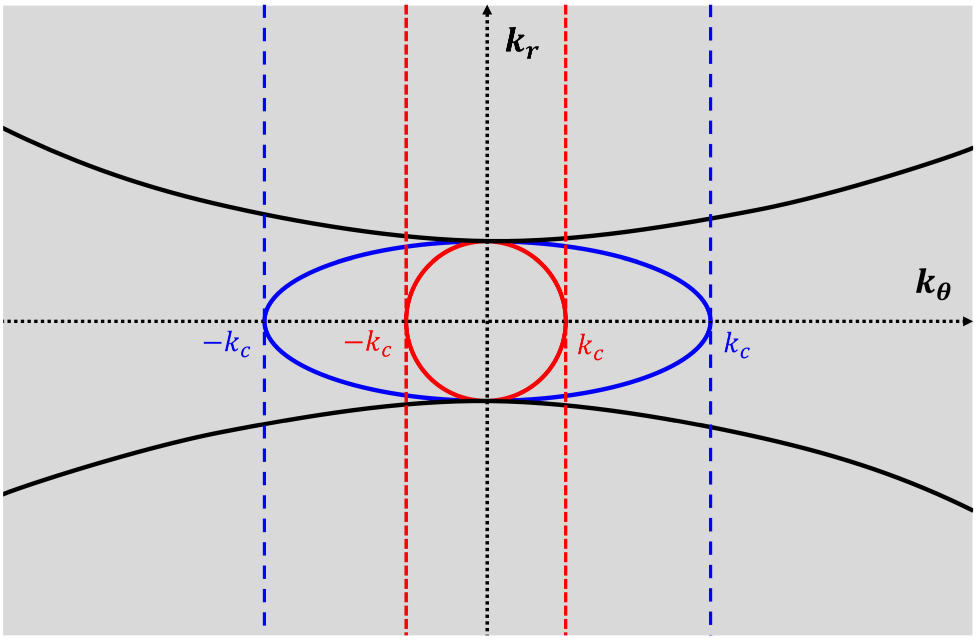

Figure 5. Schematics of spherical EFCs (red solid line), elliptic EFCs (blue solid line) and hyperbolic EFCs (black solid line). Red broken line: an unbounded area of spherical EFCs. Blue broken line: an unbounded area of elliptic EFCs. Red k_c and $-k_c$: cutoff wavevectors of spherical EFCs. Blue k_c and $-k_c$: cutoff wavevectors of elliptic EFCs.

The first hyperbolic EFC elastic hyperlens [91] used different mechanical deformation modes in two orthogonal directions to make the wave speed much slower in the θ direction than in the r direction. Because of these characteristics, the wave should not propagate along the θ direction but only in the r direction. This hyperlens (Figure 6a) was designed without local resonance structures to realize broadband operation frequency spectrum and to reduce losses. In simulations of hyperbolic EFCs for varying frequencies and width (Figure 6b), this hyperbolic hyperlens had better resolution than the previously proposed [90] elliptical hyperlens. The simulation results for their comparison were valid with a fine resolution (Figure 6c–e).

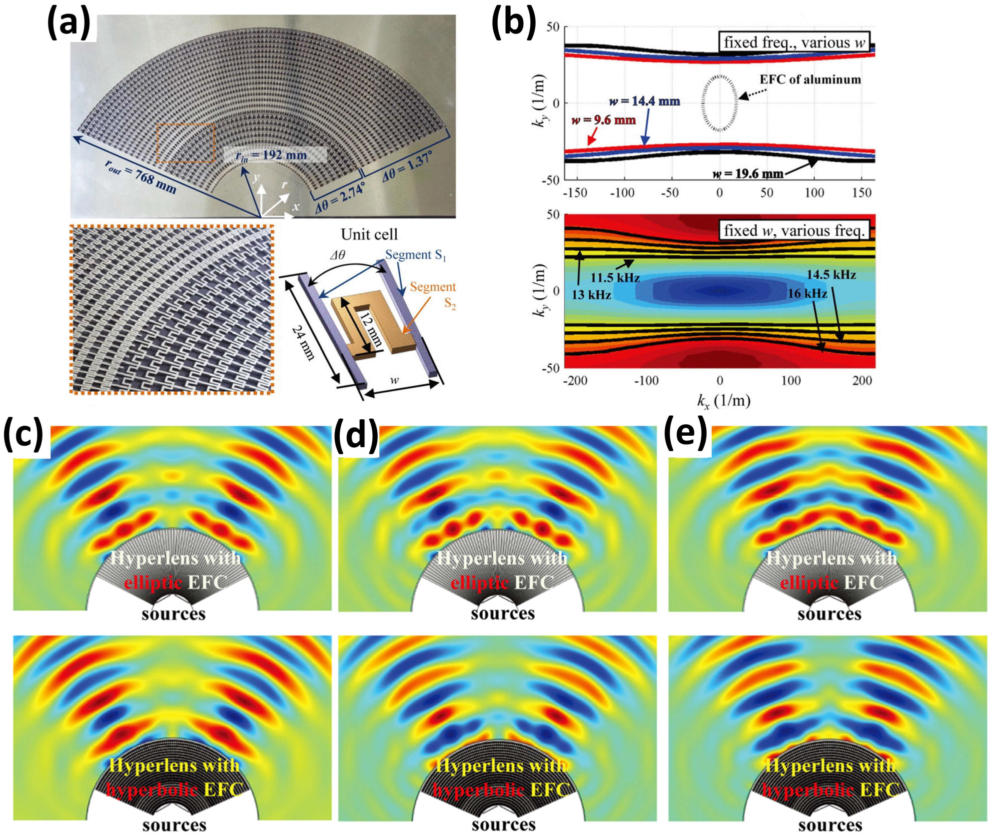

Figure 6. (**a**) Elastic hyperlens (top), close-up view (lower left) and geometry of the unit cell (lower right); (**b**) hyperbolic EFCs at 15 kHz for varying the width *w* of unit cell (upper). Hyperbolic EFCs for varying frequencies with fixed width 14.4 mm (lower); (**c**) Comparison of the hyperlenses having hyperbolic (upper) and elliptic EFCs (lower) with which the distance between two sources is 0.48λ; (**d**) 0.45λ; (**e**) 0.41λ. (**a**–**e**) adapted from [91].

Since then, due to the convenience of making a bandgap at an extremely low frequency, many studies have used internal resonance structures rather than PCs. As we mentioned in the introduction, the gap of micro-structures in PCs must be comparable to the wavelength. For this reason, it is impossible to miniaturize the structure smaller than the wavelength while making a bandgap for a low frequency (long wavelength) wave. However, in locally resonant hyper MTMs which have extreme anisotropy [92], super-resolution results from the nearly flat branch that occur before the resonance. A nearly flat dispersion curve directly below the bandgap occurred in hyperbolic MTMs implies that the magnitude of wave vectors can be significantly increased without changing the frequency. Therefore, the use of internal resonance structures can effectively reduce its size regardless of the wavelength. One EMTM lens (Figure 7a) having hyperbolic EFCs (Figure 7b) exploits anisotropic dynamic mass densities by using a resonance mechanism in the horizontal translational motion [93]. Extreme stiffness induced by the translational resonance of its local resonators compensates for the decreased effective mass density and permits total transmission and subwavelength resolution (Figure 7c). Another elastic hyperlens for a longitudinal elastic wave uses two decoupled resonators as a unit cell (Figure 7d); in numerical simulations, it achieved super-resolution of $\lambda/3$ [94]. A field that includes an elastic lens having hyperbolic EFCs (Figure 7e) induces two-directional longitudinal wave propagation (Figure 7f, top), whereas a field that does not include a hyperlens (Figure 7f, bottom) yields an omnidirectional wave [94]. A single-phase hyperbolic EMTM (Figure 7g) that exploits the anisotropy of effective mass density was optimized using a topology strategy [95]. This topology optimization realized a hyperbolic EMTM exhibiting hyperbolic EFCs (Figure 7h) that has the finest super-resolution ($\lambda/64$) to date (Figure 7i).

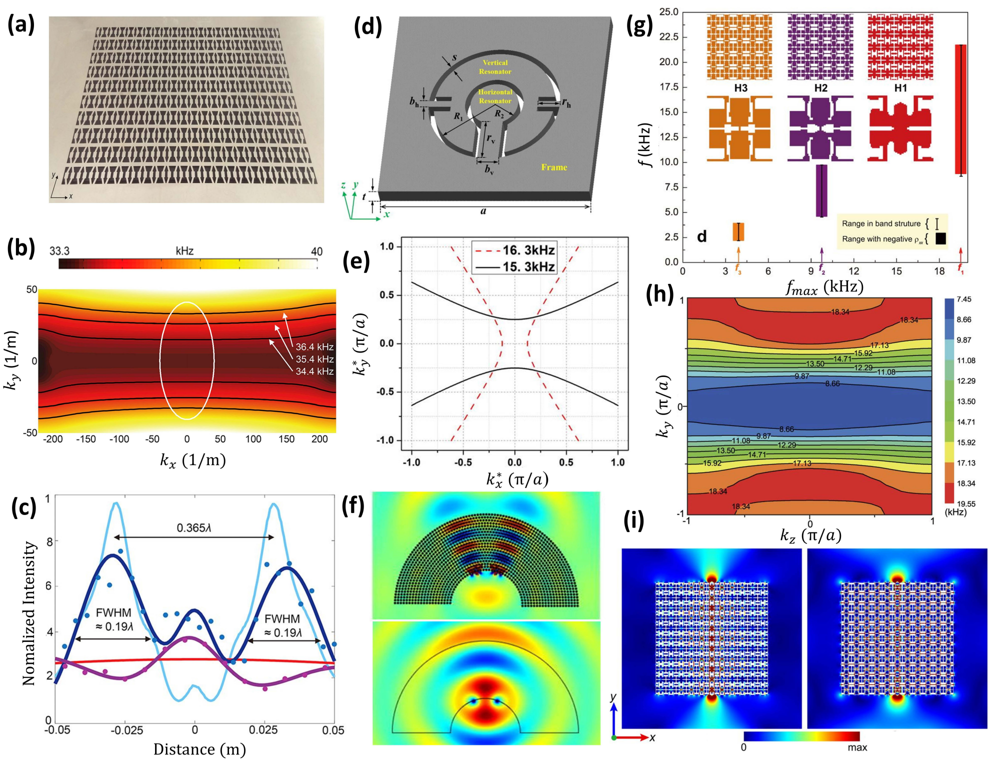

Figure 7. (**a**) Fabricated hyperbolic EMTM lens; (**b**) EFC of hyperbolic EMTM lens. White contour: equi-frequency contour of the isotropic aluminum plate at 35.48 kHz; (**c**) Intensity profiles obtained by simulation with EMTM (cyan line), without EMTM (red line) and by experiment with EMTM (blue dot) and without EMTM (purple dot). Gaussian regression was applied for experiment data (blue and purple line); (**d**) Unit cell design of EMTM; (**e**) EFC of EMTM calculated at 15.3 kHz and 16.3 kHz; (**f**) Divergence of the displacement fields with hyperlens (upper). Divergence of the displacement fields without hyperlens (lower); (**g**) Microstructures for different target frequencies (H1 at 19.5 kHz, H2 at 9.75 kHz and H3 at 3.904 kHz); (**h**) EFC of the third band for H3; (**i**) Wave propagations in H1 at 13 kHz (left) and H3 at 2.3kHz (right). The measured resolutions are 0.169λ (left) and 0.02λ (right). (**a**–**c**) adapted from [93]. (**d**–**f**) adapted from [94]. (**g**–**i**) adapted from [95].

2.4. Cloaking Elastic Waves

Cloaking has been a main topic of research since the discovery of MTMs. Initial work started in transformation optics [96,97] inspired by earlier results [98]. The characteristic that obscures an object by using electromagnetic waves is the invariance of Maxwell's equations which are as follows. Time-harmonic Maxwell's equations [99] are written as

$$\nabla \times \mathbf{E} + i\omega\boldsymbol{\mu}\mathbf{H} = 0, \quad \nabla \times \mathbf{H} + i\omega\boldsymbol{\varepsilon}\mathbf{E} = 0, \tag{5}$$

where ω is an angular frequency, $\boldsymbol{\mu}(\mathrm{x})$ is a magnetic permeability, and $\boldsymbol{\varepsilon}(\mathrm{x})$ is an electrical permittivity. Consider a mapping transformation $\mathbf{x}' = \mathbf{x}'(\mathrm{x})$, $\mathbf{E}'(\mathbf{x}') = (\mathbf{A}^T)^{-1}\mathbf{E}(\mathbf{x})$, and $\mathbf{H}'(\mathbf{x}') = (\mathbf{A}^T)^{-1}\mathbf{H}(\mathbf{x})$ where matrix $\mathbf{A}$ have elements $A_{kj} = \frac{\partial x'_k}{\partial x_j}$. Then the Maxwell's equation transforms to

$$\nabla' \times \mathbf{E}' + i\omega\boldsymbol{\mu}'\mathbf{H}' = 0, \quad \nabla' \times \mathbf{H}' + i\omega\boldsymbol{\varepsilon}'\mathbf{E}' = 0, \tag{6}$$

where $\boldsymbol{\mu}'(\mathbf{x}') = \mathbf{A}\boldsymbol{\mu}(\mathbf{x})\mathbf{A}^T/\det\mathbf{A}$ and $\boldsymbol{\varepsilon}'(\mathbf{x}') = \mathbf{A}\boldsymbol{\varepsilon}(\mathbf{x})\mathbf{A}^T/\det\mathbf{A}$. By comparing the Equations (5) and (6), it can be seen clearly that Maxwell's equations still retains their form. Most studies of transformation optics consider electromagnetic waves, but this basic principle applies equally to other types of waves, as long as the wave equation remains invariant under coordinate transformations. Therefore, cloaking has also been applied in acoustics [14,100,101]. However, the equations of motions for elastic medium do not guarantee their form-invariant and are mapped to a more general system with non-scalar density according to geometric changes [99], so cloaking of the elastic acoustic waves has been difficult to achieve with conventional methods. The propagation of a time-harmonic elastodynamic wave equation [99] is written as

$$\nabla \cdot \sigma = -\omega^2 \rho \mathbf{u}, \quad \sigma = \mathbf{C}\nabla\mathbf{u}, \tag{7}$$

where ρ is the scalar density, $\mathbf{u}$ is the displacement vector, $\mathbf{C}$ is a rank-4 elasticity tensor, $\sigma(\mathbf{x})$ is the stress field. Consider a mapping from an initial space to an arbitrary curvilinear space $\mathbf{x} \rightarrow \mathbf{x}'$ and $\mathbf{u}(\mathbf{x}) \rightarrow \mathbf{u}'(\mathbf{x}) = (\mathbf{A}^T)^{-1}\mathbf{u}(\mathbf{x})$ where $A_{ij} = \frac{\partial \mathbf{x}'_i}{\partial \mathbf{x}_j}$. Then the equation becomes

$$\nabla' \cdot \sigma' = \mathbf{D}'\nabla'\mathbf{u}' - \omega^2 \boldsymbol{\rho}'\mathbf{u}', \quad \sigma' = \mathbf{C}'\nabla'\mathbf{u}' + \mathbf{S}'\mathbf{u}', \tag{8}$$

where $\mathbf{S}'$ and $\mathbf{D}'$ are rank-3 symmetric tensors and $\boldsymbol{\rho}'$ becomes a rank-2 density tensor. Unlike the Maxwell's equation retain its form after conformal mapping (Equations (5) and (6)), it is clear that the equation after conformal mapping (Equation (8)) has a different form from Equation (7) in the elastic regime. Therefore, studies have been made to realize elastic wave cloaking for special cases by using other methods. A cylindrical cloak to control bending waves, one of several forms of elastic wave, can be achieved by a special case in a thin elastic plate [102]; the elasticity tensor can be represented by a diagonal matrix that has two non-vanishing entries. Numerical simulations (Figure 8a) suggest that a heterogeneous orthotropic thin elastic cloak can control the propagation of bending waves, and thereby extend the electromagnetic and acoustic cloaking mechanisms [103]; in corresponding experiments [104], the designed sample of elastic cloak (Figure 8b) performed well in the frequency range of 200 to 450 Hz (Figure 8c).

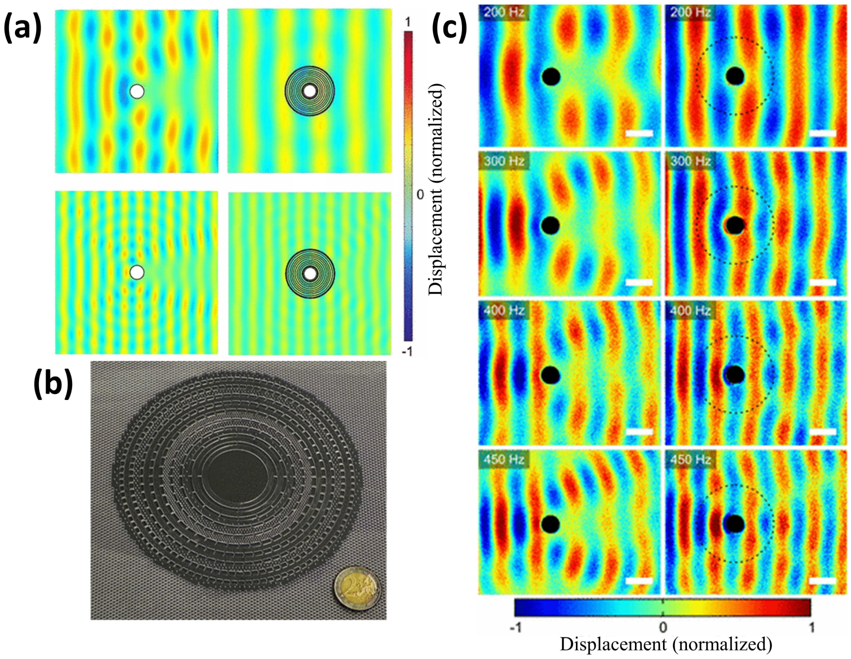

Figure 8. (**a**) Left: displacement field scattered by an obstacle for a plane wave of frequency 60 Hz (upper), 150 Hz (lower). Right: displacement field scattered by obstacle surrounded by cloak layers for a plane wave of frequency 60 Hz (upper), 150 Hz (lower); (**b**) Designed elastic cloak before filling with PDMS; (**c**) Displacement field for plane waves with frequencies of 200, 300, 400 and 450 Hz from the top. Left column: without cloak and right column: with cloak. Dashed black circles: outer radius of the cloak region; white scale bar: 5 cm. (**a**) adapted from [103]. (**b**,**c**) adapted from [104].

Another cylindrical cloak for coupled shear and longitudinal waves can be described using a rank-4 asymmetric elasticity tensor [105]. Asymmetric constitutive relations in which only the major symmetry is preserved were found by applying a cloaking transformation to Navier equations for isotropic linear elasticity. The elasticity tensor in the transformed coordinates was not fully symmetric in this study; as a result, the Navier equations remain in shape under this transformation. A generalization [106] of [99] broadens the transformation theory for elasticity. The material parameters of the transformed system were explicitly derived; they depend on both the transformation and gauge matrices, and do not necessarily have symmetric stress. Cloaking of objects from anti-plane elastic waves can be achieved by using nonlinear elastic pre-stress [107]; this approach does not require inhomogeneous anisotropic shear moduli and densities.

Nonlinear pre-stress has been proposed as a method to generate elastic cloaks [108]; a finite cloak for anti-plane elastic waves was designed by applying nonlinear pre-stress to an incompressible neo-Hookean hyper-elastic material; this method cloaked the anti-plane elastic waves (Figure 9a). An extention [109] of this idea considered a more-general elastic transformation problem that includes primary (P) and shear vertical (SV) motions, in addition to shear horizontal (SH) motion. The constitutive equations required for elastodynamics cloaking, which is restricted in the form for isotropic elasticity, were obtained; numerical simulations showed that the presence of an elastic cloak has greatly reduced scattering (Figure 9b).

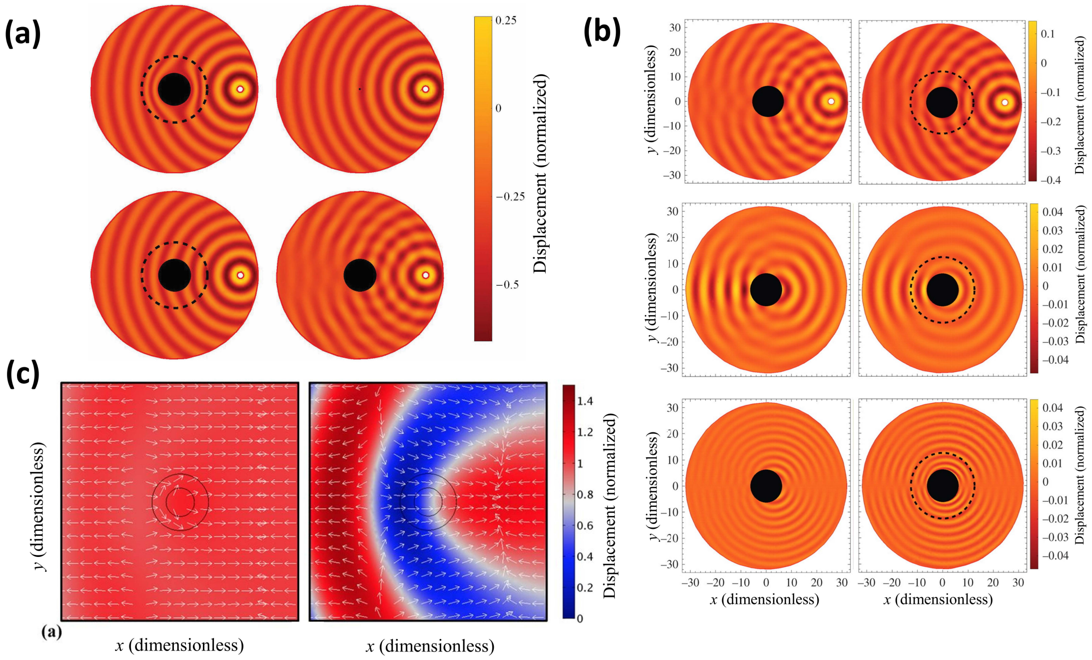

Figure 9. (**a**) Total displacement field of anti-plane shear waves. Line source is shown as a white circle. Left side: a classic elastic cloak (upper) and a designed pre-stress elastic cloak (lower). Right side: scattering from a cavity of radius $k_s R = \pi/20$ (upper) and 2π (lower) in an unstressed medium, where k_s is the shear wavenumber of the medium and R is the annulus inner radius of the cavity; (**b**) Top: Total displacement field of SH waves without a cloak (left) and with a cloak (right). Center: Scattered displacement field of P waves without a cloak (left) and with a cloak (right). Bottom: Scattered displacement field of SV waves without a cloak (left) and with a cloak (right); (**c**) Displacement field distributions of cloaked (left) and uncloaked (right) rigid object. White arrows: vector direction. Colored contours: amplitude. (**a**) adapted from [108]. (**b**) adapted from [109]. (**c**) adapted from [110].

An elastic cloak to control the scattering of bending waves in isotropic heterogeneous thin plates has also been proposed [110]. The scattering cancellation technique was applied to the biharmonic operator (∇^4) to design the cloak. A fourth-order biharmonic equation with appropriate boundary conditions to describe the propagation of bending waves in thin plates was derived from the generalized elasticity theory [111,112], and yielded the displacement field distributions of an obtained cloak (Figure 9c). A directional cloak that can protect a region from a flexural wave within a range of bandgap frequencies has been demonstrated [113]. Recently, elastic cloaking has been extended to the seismic waves that propagate through the Earth. Seismic MTMs, one of the most important application in EMTMs, are starting with the use of PCs and metasurface [35–42].

One of the ways to demonstrate elastic cloaking is to realize form-invariant Willis coupling metamaterial including an additional degree of freedom. Since it is first proposed by Willis [114], Willis coupling has been explored in elastodynamics and acoustics analogous to the bianisotropy parameter in electromagnetism. In electromagnetic metamaterials, bianisotropy enables the coupling of magnetic and electric phenomena at the subwavelength scale. In bianisotropic media, the constitutive relations in electromagnetism [115] are written as

$$\mathbf{D} = \varepsilon \mathbf{E} + \xi \mathbf{H}, \quad \mathbf{B} = \mu \mathbf{H} + \zeta \mathbf{E}, \tag{9}$$

where $\mathbf{D}$ is the electric displacement field, $\mathbf{E}$ is the electric field, $\mathbf{B}$ is the magnetic flux density field, $\mathbf{H}$ is the magnetic field, $\boldsymbol{\varepsilon}$ is the permittivity tensor and $\boldsymbol{\mu}$ is the permeability tensor. $\boldsymbol{\xi}$ and $\boldsymbol{\zeta}$ are coupling tensors. The Willis constitutive relations [114,116] can be expressed as

$$\begin{pmatrix} \langle \boldsymbol{\sigma} \rangle \\ \langle \mathbf{p} \rangle \end{pmatrix} = \begin{pmatrix} \mathbf{C}_{eff} & \mathbf{S}_{eff} \\ \tilde{\mathbf{S}}_{eff} & \boldsymbol{\rho}_{eff} \end{pmatrix} \begin{pmatrix} \langle \mathbf{e} \rangle \\ \langle \dot{\mathbf{u}} \rangle \end{pmatrix}, \tag{10}$$

where $\tilde{\mathbf{S}}_{eff}$ is the adjoint of $\mathbf{S}_{eff}$, $\mathbf{e}$ is the strain tensor, $\boldsymbol{\sigma}$ is the stress tensor, $\mathbf{C}_{eff}$ is the effective stiffness tensor, $\mathbf{u}$ is the displacement vector, $\mathbf{p}$ is the momentum density vector and $\boldsymbol{\rho}_{eff}$ is the effective mass density tensor. The overdot denotes a time derivative and $< >$ denotes the ensemble average. Note that $\mathbf{S}_{eff}$ and $\tilde{\mathbf{S}}_{eff}$ are called Willis coupling tensors. Willis coupling requires coupling between strain and momentum fields or stress and velocity fields (Equation (10)). Several approximations and simplifications to the general approach of Willis media have been published [117–123]. In fact, most studies of Willis coupling are more active in the acoustics [124–130] than in elastodynamics, but these developments in acoustics indicate that Willis metamaterial for elastic waves in solid may become practical. Recently, Willis metamaterial for flexural waves has been reported [131]. Based on a cantilever bending resonance, effective bianisotropy in a Willis metamaterial for flexural waves was designed and experimentally demonstrated.

3. Elastic Metasurfaces

Metasurfaces (MSs) are artificially-designed one-dimensional or two-dimensional equivalents of bulk MTMs. MSs are much smaller, more compact, and simpler than conventional MTMs, but can still manipulate waves. The physical mechanism of the MSs exploits adjustment of wave phase shifts, unlike bulk MTMs, in which waves are manipulated by changing the effective parameters of the material. MSs can be used in applications such as anomalous reflection and refraction [132,133], polarization conversion [134,135], focal lenses [136–138] and holograms [139–142]. MSs are based on the generalized Snell's law with phase discontinuity [143]. The generalized Snell's law of refraction is written as

$$n_t \sin(\theta_t) - n_i \sin(\theta_i) = \frac{1}{k_0} \frac{d\Phi}{dx}, \tag{11}$$

and for reflection,

$$\sin(\theta_r) - \sin(\theta_i) = \frac{1}{n_i k_0} \frac{d\Phi}{dx}, \tag{12}$$

where k_0 denotes the wavenumber of the wave and $d\Phi/dx$ denotes the phase gradient parallel to the plane, θ_i, θ_t and θ_r are the incident, transmission and reflection angle, respectively, and n_i and n_t are the refractive indices of two media (Figure 10). This law indicates that the transmitted and reflected beams can have an arbitrary direction depending on $d\Phi/dx$ as well as n_i and n_t.

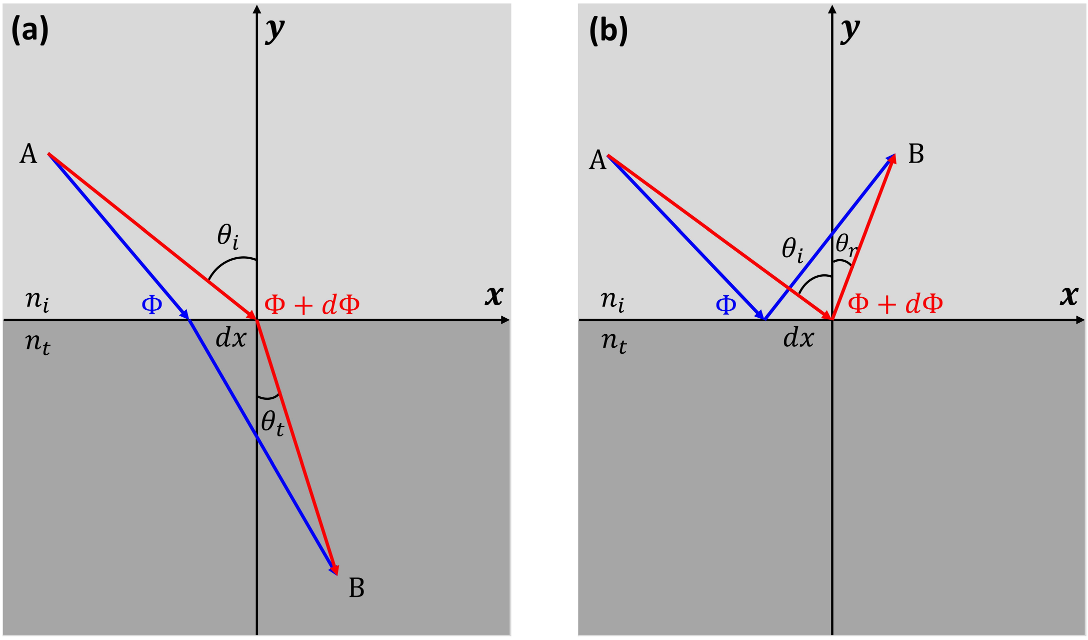

Figure 10. Schematics of the generalized Snell's law of refraction (**a**) and reflection (**b**). dx is the distance between two beams at the plane of incidence. Φ is the phase shift of the blue beam and Φ + $d\Phi$ is the phase shift of the red beam.

An elastic MS that can control both same-mode and mode-converted Lamb waves in plates has been demonstrated [144]. It is composed of locally-resonant geometric tapers; this design has the ability to control the phase shift accurately. However, the transmitted field contains unwanted wave types because of the mode conversion. This mode conversion at the material interface complicates the modulation. An elastic MS to split SV-waves and P-waves in elastic solids into different propagation directions without involving mode conversion has been proposed [145]. Transmission of SV-waves are different from those of P-waves, because the phase speed of the SV-wave only depends on the material properties while that of P-wave is susceptible to the thickness of the MS. Therefore, SV-waves can be steered while the MS remains transparent to P waves (Figure 11a,b).

An elastic MS composed of wave guides can steer the incident elastic SH waves by using an electrorheological elastomer [146]. The deflected elastic SH waves were tuned by adjusting the phase velocity that depends on the applied electric fields in the waveguides. An elastic phase-controlling elastic MS using parallel and periodically arranged-micro-sections has been demonstrated analytically and numerically [147]. Wave propagation properties depend on the periodic length of the meta-layer element at the sub-wavelength scale. The phase-controlling properties was accomplished by the frequency dependent elastic properties.

The above three studies on MSs were conducted by changing the wave velocity. However, other studies have used methods such as changing the propagation distance and adjusting local resonances. An elastic MS has been produced by changing the heights of three zigzag unit cells [148] (Figure 11c); this MS can be used in source illusion devices for shifting, transforming, and splitting a point-source (Figure 11d).

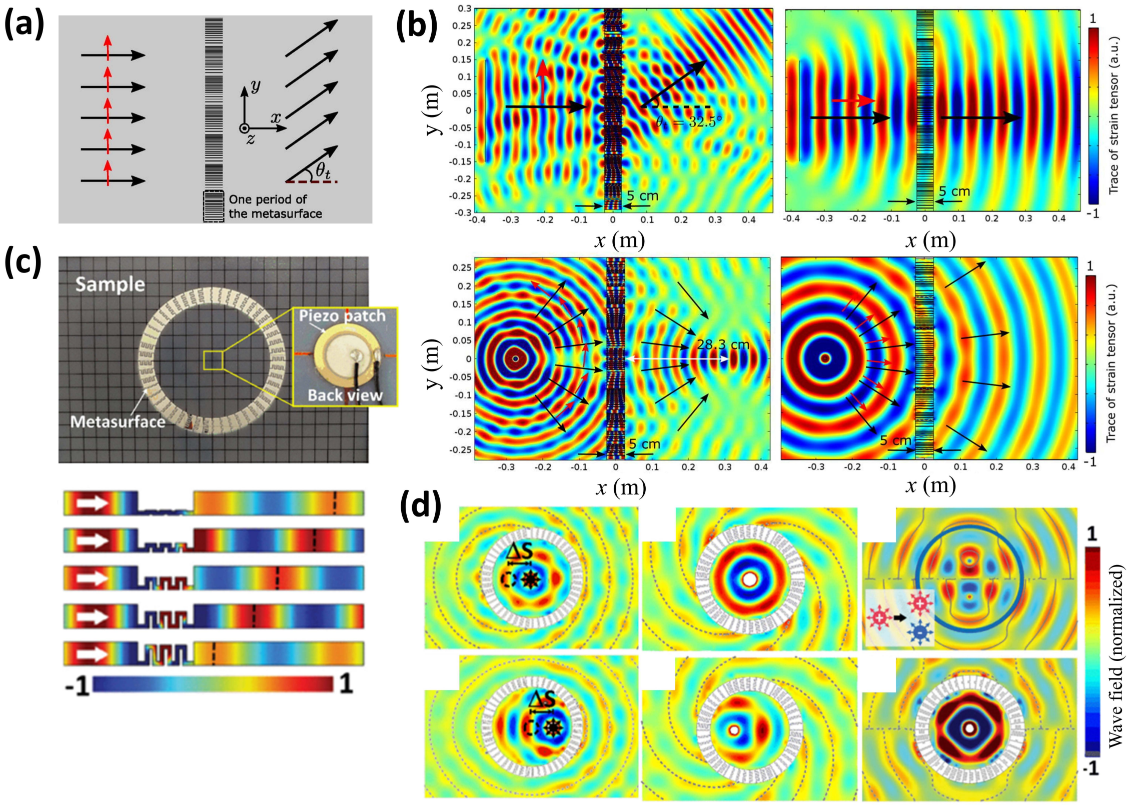

Figure 11. (**a**) Schematic of MS design; (**b**) Left side: the curl of the displacement field showing anomalous refraction of a normal incident SV-wave (upper) and focusing a cylindrical SV-wave source at 60 kHz (lower). Right side: the trace of the strain tensor showing anomalous refraction of a normal incident SV-wave (upper) and cylindrical P-wave incidence (lower) at 60 kHz; (**c**) Schematic of the source shifter (lower) and displacement field produced by different heights h of three zigzag unit cells (upper); (**d**) Left side: Source shifter; the A0 wave field at 12 kHz with the source placed at (0, 0) mm (upper) and (25, 0) mm (lower). Center side: source transformer; the A0 wave field at 8 kHz with the source placed at (0, 0) mm (upper) and (−15, 0) mm (lower). Right side: source splitter; the target profile (upper) and the experimentally-measured A0 wave field at 8 kHz (lower). (**a**,**b**) adapted from [145]. (**c**,**d**) adapted from [148].

An elastic MS has been produced by adjusting the propagation distance [149] (Figure 12a). This concept extends the concept of an acoustic MS that compensates for the lack of MTM and PCs. The designed refraction angles obtained by the numerical simulations were in excellent agreement with the analytical predictions (Figure 12b,c). An elastic MS that exploits local resonance of 3D column structures can support high transmission and full phase control to deflect flexural waves [150]. Elastic MSs can be applied to manipulate not only flexural waves but also Rayleigh and Love waves. Rayleigh waves are formed when longitudinal and transverse motions are combined and an elliptical retrograde motion emerges from a vertical plane along the direction of propagation. Love waves are formed when the horizontal particle motion is perpendicular to the direction of propagation. In seismology, both Rayleigh and Love waves are surface seismic waves produced on the Earth. MSs can applied as protective devices against seismic waves. An elastic MS which can create elastic rainbow trapping and support mode conversion of Rayleigh waves to bulk shear waves has been designed and experimentally demonstrated [40] based on the meta-wedge design [39] and the theoretical dispersion properties of an MS [36]. One elastic MS that manipulates Love waves has been demonstrated using resonators [151]. By adjusting the interaction coefficient which controls the strength of interaction between resonators and the Love waves, phase speed and n are controlled. By using this, a Luneburg and a Maxwell lens were also demonstrated in this study. An adaptive and tunable MS can manipulate elastic waves by using piezoelectric circuit integration without change in the host structure [152]; the proposed elastic MS consists of arrayed piezoelectric devices with individually-connected elements that have negative capacitance. By adjusting the negative capacitances online, discontinuous phase profiles can be obtained. A full transmission MS for in-plane longitudinal waves has also been introduced [153]; its unit cell is composed of separated substructures, so that each property is decoupled by its own geometrical parameter (Figure 12d); therefore, each substructure embedded in elastic solids behaves as a mass or as a spring element. Full transmission was achieved by breaking an intrinsic proportionally-coupled relationship between density and stiffness. The corresponding values of the discrete phase by both theoretical and experimental approach agreed well (Figure 12e).

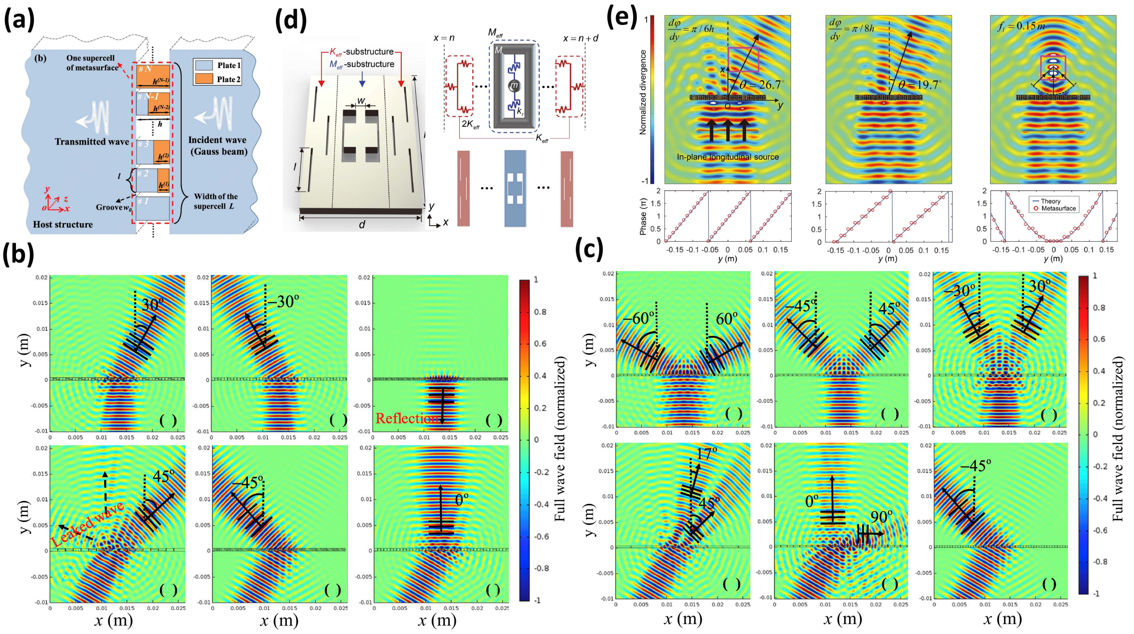

Figure 12. (**a**) Schematic of the MS. L, l, w_0 are the widths of the supercell, subunit, groove, respectively and h is the thickness of MS; (**b**) Numerical simulations of the wave field of the MS composed of four subunits. Upper side: vertical incident wave. Below side: oblique incident wave (30°). Black arrows: analytical predictions; (**c**) Numerical simulations of the wave field of the MS composed of two subunits. Upper side: vertical incident wave. Below side: oblique incident wave (30°). Black arrows: analytical predictions; (**d**) Unit cell consisting of two independent substructures (left) and the mass-spring model of the unit cell (right); (**e**) Upper side: simulation of longitudinal wave with $d\varphi/dy = \pi/6h$ (left), $d\varphi/dy = \pi/8h$ (center) and simulation of focal lens with its focal length is 0.15 m (right). Lower side: corresponding theoretical and discrete phase profile of upper side. (**a**–**c**) adapted from [149]. (**d**,**e**) adapted from [153].

4. Conclusions

MTMs present a new way to manipulate waves. However, in EMTMs, the longitudinal and transverse elastic waves are coupled, so they cannot be analyzed using techniques that apply to electromagnetic and acoustic waves. Many important technical challenges must be solved before EMTMS are appropriate for real-world applications. EMTMs manipulate and control the elastic waves by arranging micro-structures to exploit Bragg scattering or local resonance. To understand the current state of EMTMs, important studies that have been conducted are selected and represented. We introduced representative studies of locally resonant EMTMs. We explained how to handle elastic waves by using GRIN PC lenses. We have also described hyperlenses for super-resolution beyond the diffraction limit. Cloaking MTMs that effectively block elastic waves have been introduced. Also, a new budding field on Willis parameters is discussed. Elastic MSs have been introduced to overcome the limitations of existing EMTMs. In addition to these applications, EMTM-related technologies are expected to advance rapidly due to other kinds of EMTM applications such as mechanical MTMs [154,155]. This would provide deeper understanding of elastic wave manipulation, energy harvesting, super-resolution imaging, and seismic wave shielding.

Author Contributions: J.P., D.L. wrote the paper. J.R. guided the entire paper. All authors have read and agreed to the published version of the manuscript.

Funding: This work was financially supported by the K-Cloud grant (No. 2018-TECH-04) funded by the Korea Hydro & Nuclear Power Co. Ltd., Republic of Korea. This work was also partially supported from the National Research Foundation of Korea (NRF) grants (NRF-2019R1A2C3003129, CAMM-2019M3A6B3030637, NRF-2019R1A5A8080290, NRF-2018M3D1A1058998, NRF-2015R1A5A1037668) funded by the Ministry of Science and ICT (MSIT) of the Korean government. D.L. acknowledges support for the Global Ph.D. Fellowship (NRF-2018H1A2A1062053) from NRF-MSIT of the Korean government.

Acknowledgments: Special thanks to Trevon Badloe for helping to check our manuscript.

Conflicts of Interest: The authors declare no conflict of interest.

References

1. Veselago, V. Electrodynamics of substances with simultaneously negative and. *Usp. Fiz. Nauk* **1967**, *92*, 517. [CrossRef]
2. Pendry, J.B.; Holden, A.; Stewart, W.; Youngs, I. Extremely low frequency plasmons in metallic mesostructures. *Phys. Rev. Lett.* **1996**, *76*, 4773. [CrossRef]
3. Fang, N.; Lee, H.; Sun, C.; Zhang, X. Sub–diffraction-limited optical imaging with a silver superlens. *Science* **2005**, *308*, 534–537. [CrossRef]
4. Zhang, X.; Liu, Z. Superlenses to overcome the diffraction limit. *Nat. Mater.* **2008**, *7*, 435. [CrossRef]
5. Rogers, E.T.; Lindberg, J.; Roy, T.; Savo, S.; Chad, J.E.; Dennis, M.R.; Zheludev, N.I. A super-oscillatory lens optical microscope for subwavelength imaging. *Nat. Mater.* **2012**, *11*, 432. [CrossRef]
6. Cai, W.; Chettiar, U.K.; Kildishev, A.V.; Shalaev, V.M. Optical cloaking with metamaterials. *Nat. Photonics* **2007**, *1*, 224. [CrossRef]
7. Li, J.; Pendry, J.B. Hiding under the carpet: A new strategy for cloaking. *Phys. Rev. Lett.* **2008**, *101*, 203901. [CrossRef]
8. Valentine, J.; Li, J.; Zentgraf, T.; Bartal, G.; Zhang, X. An optical cloak made of dielectrics. *Nat. Mater.* **2009**, *8*, 568. [CrossRef]
9. Lal, S.; Link, S.; Halas, N.J. Nano-optics from sensing to waveguiding. *Nat. Photonics* **2007**, *1*, 641. [CrossRef]
10. O'Hara, J.F.; Singh, R.; Brener, I.; Smirnova, E.; Han, J.; Taylor, A.J.; Zhang, W. Thin-film sensing with planar terahertz metamaterials: Sensitivity and limitations. *Opt. Express* **2008**, *16*, 1786–1795. [CrossRef]
11. Kabashin, A.; Evans, P.; Pastkovsky, S.; Hendren, W.; Wurtz, G.; Atkinson, R.; Pollard, R.; Podolskiy, V.; Zayats, A. Plasmonic nanorod metamaterials for biosensing. *Nat. Mater.* **2009**, *8*, 867. [CrossRef] [PubMed]
12. Chen, T.; Li, S.; Sun, H. Metamaterials application in sensing. *Sensors* **2012**, *12*, 2742–2765. [CrossRef] [PubMed]
13. Lee, D.; Nguyen, D.M.; Rho, J. Acoustic wave science realized by metamaterials. *Nano Converg.* **2017**, *4*, 3. [CrossRef]
14. Cummer, S.A.; Schurig, D. One path to acoustic cloaking. *New J. Phys.* **2007**, *9*, 45. [CrossRef]
15. Ma, G.; Sheng, P. Acoustic metamaterials: From local resonances to broad horizons. *Sci. Adv.* **2016**, *2*, e1501595. [CrossRef]
16. Cummer, S.A.; Christensen, J.; Alù, A. Controlling sound with acoustic metamaterials. *Nat. Rev. Mater.* **2016**, *1*, 16001. [CrossRef]
17. Zhu, R.; Liu, X.; Hu, G.; Yuan, F.; Huang, G. Microstructural designs of plate-type elastic metamaterial and their potential applications: A review. *Int. J. Smart Nano Mater.* **2015**, *6*, 14–40. [CrossRef]
18. D'Alessandro, L.; Ardito, R.; Braghin, F.; Corigliano, A. Low frequency 3D ultra-wide vibration attenuation via elastic metamaterial. *Sci. Rep.* **2019**, *9*, 8039. [CrossRef]
19. Oh, J.H.; Assouar, B. Quasi-static stop band with flexural metamaterial having zero rotational stiffness. *Sci. Rep.* **2016**, *6*, 33410. [CrossRef]
20. Chen, Y.; Qian, F.; Zuo, L.; Scarpa, F.; Wang, L. Broadband and multiband vibration mitigation in lattice metamaterials with sinusoidally-shaped ligaments. *Extreme Mech. Lett.* **2017**, *17*, 24–32. [CrossRef]

21. Nobrega, E.; Gautier, F.; Pelat, A.; Dos Santos, J. Vibration band gaps for elastic metamaterial rods using wave finite element method. *Mech. Syst. Signal Proc.* **2016**, *79*, 192–202. [CrossRef]
22. Baravelli, E.; Ruzzene, M. Internally resonating lattices for bandgap generation and low-frequency vibration control. *J. Sound Vibr.* **2013**, *332*, 6562–6579. [CrossRef]
23. Sugino, C.; Ruzzene, M.; Erturk, A. Merging mechanical and electromechanical bandgaps in locally resonant metamaterials and metastructures. *J. Mech. Phys. Solids* **2018**, *116*, 323–333. [CrossRef]
24. Attarzadeh, M.; Nouh, M.; Al Ba'ba'a, H. Experimental evaluation of structural intensity in two-dimensional plate-type locally resonant elastic metamaterials. *J. Appl. Mech.* **2018**, *85*, 4.
25. Al Ba'ba'a, H.; Callanan, J.; Nouh, M. Emergence of Pseudo-Phononic Gaps in Periodically Architected Pendulums. *Front. Mater.* **2019**, *6*, 119. [CrossRef]
26. Chen, Y.; Huang, G.; Sun, C. Band gap control in an active elastic metamaterial with negative capacitance piezoelectric shunting. *J. Vib. Acoust.* **2014**, *136*, 061008. [CrossRef]
27. Nouh, M.A.; Aldraihem, O.J.; Baz, A. Periodic metamaterial plates with smart tunable local resonators. *J. Intell. Mater. Syst. Struct.* **2016**, *27*, 1829–1845. [CrossRef]
28. Zhu, R.; Chen, Y.; Barnhart, M.; Hu, G.; Sun, C.; Huang, G. Experimental study of an adaptive elastic metamaterial controlled by electric circuits. *Appl. Phys. Lett.* **2016**, *108*, 011905. [CrossRef]
29. Chen, Y.; Huang, G. Active elastic metamaterials for subwavelength wave propagation control. *Acta Mech. Sin.* **2015**, *31*, 349–363. [CrossRef]
30. Yan, X.; Zhu, R.; Huang, G.; Yuan, F.G. Focusing guided waves using surface bonded elastic metamaterials. *Appl. Phys. Lett.* **2013**, *103*, 121901. [CrossRef]
31. Chen, J.S.; Su, W.J.; Cheng, Y.; Li, W.C.; Lin, C.Y. A metamaterial structure capable of wave attenuation and concurrent energy harvesting. *J. Intell. Mater. Syst. Struct.* **2019**, *30*, 2973–2981. [CrossRef]
32. Gonella, S.; To, A.C.; Liu, W.K. Interplay between phononic bandgaps and piezoelectric microstructures for energy harvesting. *J. Mech. Phys. Solids* **2009**, *57*, 621–633. [CrossRef]
33. Hussein, M.I.; Frazier, M.J. Metadamping: An emergent phenomenon in dissipative metamaterials. *J. Sound Vibr.* **2013**, *332*, 4767–4774. [CrossRef]
34. Pope, S.A.; Daley, S. Viscoelastic locally resonant double negative metamaterials with controllable effective density and elasticity. *Phys. Lett. A* **2010**, *374*, 4250–4255. [CrossRef]
35. Brûlé, S.; Javelaud, E.H.; Enoch, S.; Guenneau, S. Experiments on seismic metamaterials: Molding surface waves. *Phys. Rev. Lett.* **2014**, *112*, 133901. [CrossRef]
36. Palermo, A.; Krödel, S.; Marzani, A.; Daraio, C. Engineered metabarrier as shield from seismic surface waves. *Sci. Rep.* **2016**, *6*, 39356. [CrossRef]
37. Achaoui, Y.; Antonakakis, T.; Brule, S.; Craster, R.; Enoch, S.; Guenneau, S. Clamped seismic metamaterials: Ultra-low frequency stop bands. *New J. Phys.* **2017**, *19*, 063022. [CrossRef]
38. Colombi, A.; Roux, P.; Guenneau, S.; Gueguen, P.; Craster, R.V. Forests as a natural seismic metamaterial: Rayleigh wave bandgaps induced by local resonances. *Sci. Rep.* **2016**, *6*, 19238. [CrossRef]
39. Colombi, A.; Colquitt, D.; Roux, P.; Guenneau, S.; Craster, R.V. A seismic metamaterial: The resonant metawedge. *Sci. Rep.* **2016**, *6*, 27717. [CrossRef]
40. Colquitt, D.; Colombi, A.; Craster, R.; Roux, P.; Guenneau, S. Seismic metasurfaces: Sub-wavelength resonators and Rayleigh wave interaction. *J. Mech. Phys. Solids* **2017**, *99*, 379–393. [CrossRef]
41. Brûlé, S.; Enoch, S.; Guenneau, S. Emergence of seismic metamaterials: Current state and future perspectives. *Phys. Lett. A* **2020**, *384*, 126034. [CrossRef]
42. Lee, D.; Oh, J.H.; Kang, I.S.; Rho, J. Seismic phononic crystals by elastodynamic Navier equation. *Phys. Rev. E* **2019**, *100*, 063002. [CrossRef]
43. Bacquet, C.L.; Ba'ba'a, H.A.; Frazier, M.J.; Nouh, M.; Hussein, M.I. Metadamping: Dissipation Emergence in Elastic Metamaterials. In *Advances in Crystals and Elastic Metamaterials, Part 1*; Hussein, M.I., Ed.; Elsevier: Amsterdam, The Netherlands, 2018; Volume 51, pp. 115–164.
44. Wang, Y.F.; Wang, Y.S.; Laude, V. Wave propagation in two-dimensional viscoelastic metamaterials. *Phys. Rev. B* **2015**, *92*, 104110. [CrossRef]
45. Attarzadeh, M.; Nouh, M. Non-reciprocal elastic wave propagation in 2D phononic membranes with spatiotemporally varying material properties. *J. Sound Vibr.* **2018**, *422*, 264–277. [CrossRef]
46. Nassar, H.; Chen, H.; Norris, A.N.; Haberman, M.R.; Huang, G.L. Non-reciprocal wave propagation in modulated elastic metamaterials. *Proc. R. Soc. A-Math. Phys. Eng. Sci.* **2017**, *473*, 20170188. [CrossRef]

47. Attarzadeh, M.; Callanan, J.; Nouh, M. Experimental Observation of Non-reciprocal Waves in a Resonant Metamaterial Beam. *arXiv* **2019**, arXiv:1910.08765.
48. Nash, L.M.; Kleckner, D.; Read, A.; Vitelli, V.; Turner, A.M.; Irvine, W.T. Topological mechanics of gyroscopic metamaterials. *Proc. Natl. Acad. Sci. USA* **2015**, *112*, 14495–14500. [CrossRef]
49. Attarzadeh, M.A.; Maleki, S.; Crassidis, J.L.; Nouh, M. Non-reciprocal wave phenomena in energy self-reliant gyric metamaterials. *J. Acoust. Soc. Am.* **2019**, *146*, 789–801. [CrossRef]
50. Mousavi, S.H.; Khanikaev, A.B.; Wang, Z. Topologically protected elastic waves in phononic metamaterials. *Nat. Commun.* **2015**, *6*, 8682. [CrossRef]
51. Wang, P.; Lu, L.; Bertoldi, K. Topological Phononic Crystals with One-Way Elastic Edge Waves. *Phys. Rev. Lett.* **2015**, *115*, 104302. [CrossRef]
52. Wu, Y.; Lai, Y.; Zhang, Z.Q. Effective medium theory for elastic metamaterials in two dimensions. *Phys. Rev. B* **2007**, *76*, 205313. [CrossRef]
53. Torrent, D.; Pennec, Y.; Djafari-Rouhani, B. Effective medium theory for elastic metamaterials in thin elastic plates. *Phys. Rev. B* **2014**, *90*, 104110. [CrossRef]
54. Lee, H.J.; Lee, H.S.; Ma, P.S.; Kim, Y.Y. Effective material parameter retrieval of anisotropic elastic metamaterials with inherent nonlocality. *J. Appl. Phys.* **2016**, *120*, 104902. [CrossRef]
55. Lai, Y.; Wu, Y.; Sheng, P.; Zhang, Z.Q. Hybrid elastic solids. *Nat. Mater.* **2011**, *10*, 620. [CrossRef] [PubMed]
56. Wu, Y.; Lai, Y.; Zhang, Z.Q. Elastic Metamaterials with Simultaneously Negative Effective Shear Modulus and Mass Density. *Phys. Rev. Lett.* **2011**, *107*, 105506. [CrossRef] [PubMed]
57. Zhu, R.; Liu, X.; Hu, G.; Sun, C.; Huang, G. Negative refraction of elastic waves at the deep-subwavelength scale in a single-phase metamaterial. *Nat. Commun.* **2014**, *5*, 5510. [CrossRef]
58. Ma, G.; Fu, C.; Wang, G.; Del Hougne, P.; Christensen, J.; Lai, Y.; Sheng, P. Polarization bandgaps and fluid-like elasticity in fully solid elastic metamaterials. *Nat. Commun.* **2016**, *7*, 13536. [CrossRef]
59. Lucklum, R. Phononic Crystals and Metamaterials–Promising New Sensor Platforms. *Procedia Eng.* **2014**, *87*, 40–45. [CrossRef]
60. Lu, M.H.; Feng, L.; Chen, Y.F. Phononic crystals and acoustic metamaterials. *Mater. Today* **2009**, *12*, 34–42. [CrossRef]
61. Kushwaha, M.S.; Halevi, P.; Dobrzynski, L.; Djafari-Rouhani, B. Acoustic band structure of periodic elastic composites. *Phys. Rev. Lett.* **1993**, *71*, 2022. [CrossRef]
62. Lucklum, R.; Li, J. Phononic crystals for liquid sensor applications. *Meas. Sci. Technol.* **2009**, *20*, 124014. [CrossRef]
63. Lucklum, R.; Ke, M.; Zubtsov, M. Two-dimensional phononic crystal sensor based on a cavity mode. *Sens. Actuator B-Chem.* **2012**, *171*, 271–277. [CrossRef]
64. Zubtsov, M.; Lucklum, R.; Ke, M.; Oseev, A.; Grundmann, R.; Henning, B.; Hempel, U. 2D phononic crystal sensor with normal incidence of sound. *Sens. Actuator A-Phys.* **2012**, *186*, 118–124. [CrossRef]
65. Oseev, A.; Zubtsov, M.; Lucklum, R. Gasoline properties determination with phononic crystal cavity sensor. *Sens. Actuator B-Chem.* **2013**, *189*, 208–212. [CrossRef]
66. Khelif, A.; Deymier, P.A.; Djafari-Rouhani, B.; Vasseur, J.; Dobrzynski, L. Two-dimensional phononic crystal with tunable narrow pass band: Application to a waveguide with selective frequency. *J. Appl. Phys.* **2003**, *94*, 1308–1311. [CrossRef]
67. Pennec, Y.; Djafari-Rouhani, B.; Vasseur, J.; Khelif, A.; Deymier, P.A. Tunable filtering and demultiplexing in phononic crystals with hollow cylinders. *Phys. Rev. E* **2004**, *69*, 046608. [CrossRef]
68. Qiu, C.; Liu, Z.; Mei, J.; Shi, J. Mode-selecting acoustic filter by using resonant tunneling of two-dimensional double phononic crystals. *Appl. Phys. Lett.* **2005**, *87*, 104101. [CrossRef]
69. Khelif, A.; Choujaa, A.; Benchabane, S.; Djafari-Rouhani, B.; Laude, V. Guiding and bending of acoustic waves in highly confined phononic crystal waveguides. *Appl. Phys. Lett.* **2004**, *84*, 4400–4402. [CrossRef]
70. Sun, J.H.; Wu, T.T. Propagation of surface acoustic waves through sharply bent two-dimensional phononic crystal waveguides using a finite-difference time-domain method. *Phys. Rev. B* **2006**, *74*, 174305. [CrossRef]
71. Vasseur, J.; Hladky-Hennion, A.C.; Djafari-Rouhani, B.; Duval, F.; Dubus, B.; Pennec, Y.; Deymier, P.A. Waveguiding in two-dimensional piezoelectric phononic crystal plates. *J. Appl. Phys.* **2007**, *101*, 114904. [CrossRef]
72. Lin, S.C.S.; Huang, T.J.; Sun, J.H.; Wu, T.T. Gradient-index phononic crystals. *Phys. Rev. B* **2009**, *79*, 094302. [CrossRef]

73. Wu, T.T.; Chen, Y.T.; Sun, J.H.; Lin, S.C.S.; Huang, T.J. Focusing of the lowest antisymmetric Lamb wave in a gradient-index phononic crystal plate. *Appl. Phys. Lett.* **2011**, *98*, 171911. [CrossRef]
74. Zhao, J.; Marchal, R.; Bonello, B.; Boyko, O. Efficient focalization of antisymmetric Lamb waves in gradient-index phononic crystal plates. *Appl. Phys. Lett.* **2012**, *101*, 261905. [CrossRef]
75. Chiou, M.J.; Lin, Y.C.; Ono, T.; Esashi, M.; Yeh, S.L.; Wu, T.T. Focusing and waveguiding of Lamb waves in micro-fabricated piezoelectric phononic plates. *Ultrasonics* **2014**, *54*, 1984–1990. [CrossRef]
76. Jin, Y.; Torrent, D.; Pennec, Y.; Pan, Y.; Djafari-Rouhani, B. Simultaneous control of the S 0 and A 0 Lamb modes by graded phononic crystal plates. *J. Appl. Phys.* **2015**, *117*, 244904. [CrossRef]
77. Zhao, J.; Bonello, B.; Becerra, L.; Boyko, O.; Marchal, R. Focusing of Rayleigh waves with gradient-index phononic crystals. *Appl. Phys. Lett.* **2016**, *108*, 221905. [CrossRef]
78. Climente, A.; Torrent, D.; Sánchez-Dehesa, J. Gradient index lenses for flexural waves based on thickness variations. *Appl. Phys. Lett.* **2014**, *105*, 064101. [CrossRef]
79. Colombi, A. Resonant metalenses for flexural waves in plates. *J. Acoust. Soc. Am.* **2016**, *140*, EL423–EL428. [CrossRef]
80. Kim, S.H. Retroreflector approximation of a generalized Eaton lens. *J. Mod. Opt.* **2012**, *59*, 839–842. [CrossRef]
81. Lee, D.; Cho, C.; Mun, J.; Park, N.; Rho, J. Demonstration of steering acoustic waves by generalized Eaton lens. *Appl. Phys. Lett.* **2018**, *113*, 161904. [CrossRef]
82. Tol, S.; Degertekin, F.; Erturk, A. Gradient-index phononic crystal lens-based enhancement of elastic wave energy harvesting. *Appl. Phys. Lett.* **2016**, *109*, 063902. [CrossRef]
83. Zareei, A.; Darabi, A.; Leamy, M.J.; Alam, M.R. Continuous profile flexural GRIN lens: Focusing and harvesting flexural waves. *Appl. Phys. Lett.* **2018**, *112*, 023901. [CrossRef]
84. Tol, S.; Degertekin, F.; Erturk, A. Phononic crystal Luneburg lens for omnidirectional elastic wave focusing and energy harvesting. *Appl. Phys. Lett.* **2017**, *111*, 013503. [CrossRef]
85. Rho, J.; Ye, Z.; Xiong, Y.; Yin, X.; Liu, Z.; Choi, H.; Bartal, G.; Zhang, X. Spherical hyperlens for two-dimensional sub-diffractional imaging at visible frequencies. *Nat. Commun.* **2010**, *1*, 143. [CrossRef] [PubMed]
86. Lu, D.; Liu, Z. Hyperlenses and metalenses for far-field super-resolution imaging. *Nat. Commun.* **2012**, *3*, 1205. [CrossRef] [PubMed]
87. Poddubny, A.; Iorsh, I.; Belov, P.; Kivshar, Y. Hyperbolic metamaterials. *Nat. Photonics* **2013**, *7*, 948. [CrossRef]
88. Jacob, Z.; Alekseyev, L.V.; Narimanov, E. Optical hyperlens: Far-field imaging beyond the diffraction limit. *Opt. Express* **2006**, *14*, 8247–8256. [CrossRef]
89. Li, J.; Fok, L.; Yin, X.; Bartal, G.; Zhang, X. Experimental demonstration of an acoustic magnifying hyperlens. *Nat. Mater.* **2009**, *8*, 931. [CrossRef]
90. Lee, H.J.; Kim, H.W.; Kim, Y.Y. Far-field subwavelength imaging for ultrasonic elastic waves in a plate using an elastic hyperlens. *Appl. Phys. Lett.* **2011**, *98*, 241912. [CrossRef]
91. Oh, J.H.; Min Seung, H.; Young Kim, Y. A truly hyperbolic elastic metamaterial lens. *Appl. Phys. Lett.* **2014**, *104*, 073503. [CrossRef]
92. Colombi, A.; Craster, R.V.; Colquitt, D.; Achaoui, Y.; Guenneau, S.; Roux, P.; Rupin, M. Elastic wave control beyond band-gaps: Shaping the flow of waves in plates and half-spaces with subwavelength resonant rods. *Front. Mech. Eng.* **2017**, *3*, 10. [CrossRef]
93. Lee, H.; Oh, J.H.; Seung, H.M.; Cho, S.H.; Kim, Y.Y. Extreme stiffness hyperbolic elastic metamaterial for total transmission subwavelength imaging. *Sci. Rep.* **2016**, *6*, 24026. [CrossRef] [PubMed]
94. Zhu, R.; Chen, Y.; Wang, Y.; Hu, G.; Huang, G. A single-phase elastic hyperbolic metamaterial with anisotropic mass density. *J. Acoust. Soc. Am.* **2016**, *139*, 3303–3310. [CrossRef] [PubMed]
95. Dong, H.W.; Zhao, S.D.; Wang, Y.S.; Zhang, C. Broadband single-phase hyperbolic elastic metamaterials for super-resolution imaging. *Sci. Rep.* **2018**, *8*, 2247. [CrossRef] [PubMed]
96. Pendry, J.B.; Schurig, D.; Smith, D.R. Controlling electromagnetic fields. *Science* **2006**, *312*, 1780–1782. [CrossRef] [PubMed]
97. Leonhardt, U. Optical conformal mapping. *Science* **2006**, *312*, 1777–1780. [CrossRef]
98. Greenleaf, A.; Lassas, M.; Uhlmann, G. On nonuniqueness for Calderon’s inverse problem. *Math. Res. Lett.* **2003**, *10*, 685–693. [CrossRef]
99. Milton, G.W.; Briane, M.; Willis, J.R. On cloaking for elasticity and physical equations with a transformation invariant form. *New J. Phys.* **2006**, *8*, 248. [CrossRef]

100. Chen, H.; Chan, C. Acoustic cloaking in three dimensions using acoustic metamaterials. *Appl. Phys. Lett.* **2007**, *91*, 183518. [CrossRef]
101. Zhang, S.; Xia, C.; Fang, N. Broadband Acoustic Cloak for Ultrasound Waves. *Phys. Rev. Lett.* **2011**, *106*, 024301. [CrossRef]
102. Farhat, M.; Guenneau, S.; Enoch, S.; Movchan, A.B. Cloaking bending waves propagating in thin elastic plates. *Phys. Rev. B* **2009**, *79*, 033102. [CrossRef]
103. Farhat, M.; Guenneau, S.; Enoch, S. Ultrabroadband elastic cloaking in thin plates. *Phys. Rev. Lett.* **2009**, *103*, 024301. [CrossRef] [PubMed]
104. Stenger, N.; Wilhelm, M.; Wegener, M. Experiments on elastic cloaking in thin plates. *Phys. Rev. Lett.* **2012**, *108*, 014301. [CrossRef] [PubMed]
105. Brun, M.; Guenneau, S.; Movchan, A.B. Achieving control of in-plane elastic waves. *Appl. Phys. Lett.* **2009**, *94*, 061903. [CrossRef]
106. Norris, A.N.; Shuvalov, A.L. Elastic cloaking theory. *Wave Motion* **2011**, *48*, 525–538. [CrossRef]
107. Parnell, W.J. Nonlinear pre-stress for cloaking from antiplane elastic waves. *Proc. R. Soc. A-Math. Phys. Eng. Sci.* **2011**, *468*, 563–580. [CrossRef]
108. Parnell, W.J.; Norris, A.N.; Shearer, T. Employing pre-stress to generate finite cloaks for antiplane elastic waves. *Appl. Phys. Lett.* **2012**, *100*, 171907. [CrossRef]
109. Norris, A.N.; Parnell, W.J. Hyperelastic cloaking theory: Transformation elasticity with pre-stressed solids. *Proc. R. Soc. A-Math. Phys. Eng. Sci.* **2012**, *468*, 2881–2903. [CrossRef]
110. Farhat, M.; Chen, P.Y.; Bağcı, H.; Enoch, S.; Guenneau, S.; Alu, A. Platonic scattering cancellation for bending waves in a thin plate. *Sci. Rep.* **2014**, *4*, 4644. [CrossRef]
111. Timoshenko, S.P.; Woinowsky-Krieger, S. *Theory of Plates and Shells*; McGraw-Hill: New York, NY, USA, 1959.
112. Graff, K.F. *Wave Motion in Elastic Solids*; Courier Corporation: North Chelmsford, MA, USA, 2012.
113. Colombi, A.; Roux, P.; Guenneau, S.; Rupin, M. Directional cloaking of flexural waves in a plate with a locally resonant metamaterial. *J. Acoust. Soc. Am.* **2015**, *137*, 1783–1789. [CrossRef]
114. Willis, J. Variational principles for dynamic problems for inhomogeneous elastic media. *Wave Motion* **1981**, *3*, 1–11. [CrossRef]
115. Marqués, R.; Medina, F.; Rafii-El-Idrissi, R. Role of bianisotropy in negative permeability and left-handed metamaterials. *Phys. Rev. B* **2002**, *65*, 144440. [CrossRef]
116. Milton, G.W.; Willis, J.R. On modifications of Newton's second law and linear continuum elastodynamics. *Proc. R. Soc. A-Math. Phys. Eng. Sci.* **2007**, *463*, 855–880. [CrossRef]
117. Nemat-Nasser, S.; Srivastava, A. Overall dynamic constitutive relations of layered elastic composites. *J. Mech. Phys. Solids* **2011**, *59*, 1953–1965. [CrossRef]
118. Srivastava, A.; Nemat-Nasser, S. Overall dynamic properties of three-dimensional periodic elastic composites. *Proc. R. Soc. A-Math. Phys. Eng. Sci.* **2012**, *468*, 269–287. [CrossRef]
119. Norris, A.N.; Shuvalov, A.L.; Kutsenko, A.A. Analytical formulation of three-dimensional dynamic homogenization for periodic elastic systems. *Proc. R. Soc. A-Math. Phys. Eng. Sci.* **2012**, *468*, 1629–1651. [CrossRef]
120. Sieck, C.F.; Alù, A.; Haberman, M.R. Dynamic Homogenization of Acoustic Metamaterials with Coupled Field Response. *Phys. Proc.* **2015**, *70*, 275–278. [CrossRef]
121. Muhlestein, M.B.; Sieck, C.F.; Alù, A.; Haberman, M.R. Reciprocity, passivity and causality in Willis materials. *Proc. R. Soc. A-Math. Phys. Eng. Sci.* **2016**, *472*, 20160604. [CrossRef]
122. Xiang, Z.; Yao, R. Realizing the Willis equations with pre-stresses. *J. Mech. Phys. Solids* **2016**, *87*, 1–6. [CrossRef]
123. Nassar, H.; Xu, X.; Norris, A.; Huang, G. Modulated phononic crystals: Non-reciprocal wave propagation and Willis materials. *J. Mech. Phys. Solids* **2017**, *101*, 10–29. [CrossRef]
124. Koo, S.; Cho, C.; Jeong, J.h.; Park, N. Acoustic omni meta-atom for decoupled access to all octants of a wave parameter space. *Nat. Commun.* **2016**, *7*, 13012. [CrossRef] [PubMed]
125. Muhlestein, M.B.; Sieck, C.F.; Wilson, P.S.; Haberman, M.R. Experimental evidence of Willis coupling in a one-dimensional effective material element. *Nat. Commun.* **2017**, *8*, 15625. [CrossRef] [PubMed]
126. Sieck, C.F.; Alù, A.; Haberman, M.R. Origins of Willis coupling and acoustic bianisotropy in acoustic metamaterials through source-driven homogenization. *Phys. Rev. B* **2017**, *96*, 104303. [CrossRef]

127. Li, J.; Shen, C.; Díaz-Rubio, A.; Tretyakov, S.A.; Cummer, S.A. Systematic design and experimental demonstration of bianisotropic metasurfaces for scattering-free manipulation of acoustic wavefronts. *Nat. Commun.* **2018**, *9*, 1342. [CrossRef] [PubMed]
128. Quan, L.; Ra'di, Y.; Sounas, D.L.; Alù, A. Maximum Willis Coupling in Acoustic Scatterers. *Phys. Rev. Lett.* **2018**, *120*, 254301. [CrossRef] [PubMed]
129. Quan, L.; Sounas, D.L.; Alù, A. Nonreciprocal Willis Coupling in Zero-Index Moving Media. *Phys. Rev. Lett.* **2019**, *123*, 064301. [CrossRef] [PubMed]
130. Melnikov, A.; Chiang, Y.K.; Quan, L.; Oberst, S.; Alù, A.; Marburg, S.; Powell, D. Acoustic meta-atom with experimentally verified maximum Willis coupling. *Nat. Commun.* **2019**, *10*, 1–7. [CrossRef]
131. Liu, Y.; Liang, Z.; Zhu, J.; Xia, L.; Mondain-Monval, O.; Brunet, T.; Alù, A.; Li, J. Willis Metamaterial on a Structured Beam. *Phys. Rev. X* **2019**, *9*, 011040. [CrossRef]
132. Ni, X.; Emani, N.K.; Kildishev, A.V.; Boltasseva, A.; Shalaev, V.M. Broadband light bending with plasmonic nanoantennas. *Science* **2012**, *335*, 427. [CrossRef]
133. Sun, S.; Yang, K.Y.; Wang, C.M.; Juan, T.K.; Chen, W.T.; Liao, C.Y.; He, Q.; Xiao, S.; Kung, W.T.; Guo, G.Y.; et al. High-efficiency broadband anomalous reflection by gradient meta-surfaces. *Nano Lett.* **2012**, *12*, 6223–6229. [CrossRef]
134. Zhu, H.; Cheung, S.; Chung, K.L.; Yuk, T.I. Linear-to-circular polarization conversion using metasurface. *IEEE Trans. Antennas Propag.* **2013**, *61*, 4615–4623. [CrossRef]
135. Arbabi, A.; Horie, Y.; Bagheri, M.; Faraon, A. Dielectric metasurfaces for complete control of phase and polarization with subwavelength spatial resolution and high transmission. *Nat. Nanotechnol.* **2015**, *10*, 937. [CrossRef] [PubMed]
136. Li, X.; Xiao, S.; Cai, B.; He, Q.; Cui, T.J.; Zhou, L. Flat metasurfaces to focus electromagnetic waves in reflection geometry. *Opt. Lett.* **2012**, *37*, 4940–4942. [CrossRef] [PubMed]
137. Aieta, F.; Genevet, P.; Kats, M.A.; Yu, N.; Blanchard, R.; Gaburro, Z.; Capasso, F. Aberration-free ultrathin flat lenses and axicons at telecom wavelengths based on plasmonic metasurfaces. *Nano Lett.* **2012**, *12*, 4932–4936. [CrossRef] [PubMed]
138. West, P.R.; Stewart, J.L.; Kildishev, A.V.; Shalaev, V.M.; Shkunov, V.V.; Strohkendl, F.; Zakharenkov, Y.A.; Dodds, R.K.; Byren, R. All-dielectric subwavelength metasurface focusing lens. *Opt. Express* **2014**, *22*, 26212–26221. [CrossRef]
139. Zheng, G.; Mühlenbernd, H.; Kenney, M.; Li, G.; Zentgraf, T.; Zhang, S. Metasurface holograms reaching 80% efficiency. *Nat. Nanotechnol.* **2015**, *10*, 308. [CrossRef]
140. Li, Z.; Kim, I.; Zhang, L.; Mehmood, M.Q.; Anwar, M.S.; Saleem, M.; Lee, D.; Nam, K.T.; Zhang, S.; Luk'yanchuk, B.; et al. Dielectric Meta-Holograms Enabled with Dual Magnetic Resonances in Visible Light. *ACS Nano* **2017**, *11*, 9382–9389. [CrossRef]
141. Yoon, G.; Lee, D.; Nam, K.T.; Rho, J. Pragmatic metasurface hologram at visible wavelength: The balance between diffraction efficiency and fabrication compatibility. *ACS Photonics* **2017**, *5*, 1643–1647. [CrossRef]
142. Ansari, M.A.; Kim, I.; Lee, D.; Waseem, M.H.; Zubair, M.; Mahmood, N.; Badloe, T.; Yerci, S.; Tauqeer, T.; Mehmood, M.Q.; et al. A Spin-Encoded All-Dielectric Metahologram for Visible Light. *Laser Photon. Rev.* **2019**, *13*, 1900065. [CrossRef]
143. Yu, N.; Genevet, P.; Kats, M.A.; Aieta, F.; Tetienne, J.P.; Capasso, F.; Gaburro, Z. Light Propagation with Phase Discontinuities: Generalized Laws of Reflection and Refraction. *Science* **2011**, *334*, 333–337. [CrossRef]
144. Zhu, H.; Semperlotti, F. Anomalous Refraction of Acoustic Guided Waves in Solids with Geometrically Tapered Metasurfaces. *Phys. Rev. Lett.* **2016**, *117*, 034302. [CrossRef] [PubMed]
145. Su, X.; Lu, Z.; Norris, A.N. Elastic metasurfaces for splitting SV- and P-waves in elastic solids. *J. Appl. Phys.* **2018**, *123*, 091701. [CrossRef]
146. Xu, Y.; Li, Y.; Cao, L.; Yang, Z.; Zhou, X. Steering of SH wave propagation in electrorheological elastomer with a structured meta-slab by tunable phase discontinuities. *AIP Adv.* **2017**, *7*, 095114. [CrossRef]
147. Shen, X.; Sun, C.T.; Barnhart, M.V.; Huang, G. Elastic wave manipulation by using a phase-controlling meta-layer. *J. Appl. Phys.* **2018**, *123*, 091708. [CrossRef]
148. Liu, Y.; Liang, Z.; Liu, F.; Diba, O.; Lamb, A.; Li, J. Source Illusion Devices for Flexural Lamb Waves Using Elastic Metasurfaces. *Phys. Rev. Lett.* **2017**, *119*, 034301. [CrossRef]
149. Cao, L.; Yang, Z.; Xu, Y. Steering elastic SH waves in an anomalous way by metasurface. *J. Sound Vibr.* **2018**, *418*, 1–14. [CrossRef]

150. Cao, L.; Yang, Z.; Xu, Y.; Assouar, B. Deflecting flexural wave with high transmission by using pillared elastic metasurface. *Smart Mater. Struct.* **2018**, *27*, 075051. [CrossRef]
151. Palermo, A.; Marzani, A. Control of Love waves by resonant metasurfaces. *Sci. Rep.* **2018**, *8*, 7234. [CrossRef]
152. Li, S.; Xu, J.; Tang, J. Tunable modulation of refracted lamb wave front facilitated by adaptive elastic metasurfaces. *Appl. Phys. Lett.* **2018**, *112*, 021903. [CrossRef]
153. Lee, H.; Lee, J.K.; Seung, H.M.; Kim, Y.Y. Mass-Stiffness substructuring of an elastic metasurface for full transmission beam steering. *J. Mech. Phys. Solids* **2018**, *112*, 577–593. [CrossRef]
154. Bertoldi, K.; Vitelli, V.; Christensen, J.; van Hecke, M. Flexible mechanical metamaterials. *Nat. Rev. Mater.* **2017**, *2*, 17066. [CrossRef]
155. Surjadi, J.U.; Gao, L.; Du, H.; Li, X.; Xiong, X.; Fang, N.X.; Lu, Y. Mechanical Metamaterials and Their Engineering Applications. *Adv. Eng. Mater.* **2019**, *21*, 1800864. [CrossRef]